國立交通大學

電子工程學系　　電子研究所

碩 士 論 文

馬西森定則在金氧半場效電晶體電子通用遷移率造成的誤差並其修正

The Error of Matthiessen's Rule in MOSFET electron Universal Mobility and Its Correction

研究生: 黃怡惠 Yi-Hui Huang

指導教授: 陳明哲 博士 Prof. Ming-Jer Chen

中華民國 一0一年 十 月

馬西森定則在金氧半場效電晶體電子通用遷移率造成的誤差並其修正

The Error of Matthiessen's Rule in MOSFET electron Universal Mobility and Its Correction

研究生: 黃怡惠 Yi-Hui Huang

指導教授: 陳明哲 博士 Prof. Ming-Jer Chen

國立交通大學

電子工程學系　電子研究所

碩士論文

A Thesis

Submitted to Department of Electronics Engineering &

Institute of Electronics

College of Electrical and Computer Engineering

National Chiao Tung University

in Partial Fulfillment of the Requirements

for the Degree of

Master of Science

in

Electronics Engineering

October 2012

Hsinchu, Taiwan, Republic of China

中華民國 一0一 年 十 月

馬西森定則在金氧半場效電晶體電子通用遷移率造成的誤差並其修正

研究生: 黃怡惠　　指導教授: 陳明哲 博士

國立交通大學

電子工程學系 電子研究所碩士班

摘要

本篇論文主旨係分析利用馬西森定則計算使用平面場效電晶體量子模擬器模擬得到的電子通用遷移率與使用馬西森定則計算萃取的電子通用遷移率之間的誤差。此研究方法主要專注於高電場區域，通用的遷移率含有兩種不同的散射機制(1)聲子散射所造成的遷移率與(2)表面粗糙度散射所造成的遷移率。通過實驗驗證組成的自洽求解薛丁格方程式與卜松方程式以及通用遷移率的模擬程式的使用，我們嘗試修正使用馬西森定則來求得金氧半場效電晶體的遷移率所造成的實驗誤差。而此修正過的定則的核心在於物理的半經驗模型，並且可以使用最低能帶的佔有率與各個遷移率的組成來明確表示使用傳統馬西森定則所造成的誤差。此新的模型可以在實際的條件下成立(溫度高達 400K)並且可應用在廣泛的基底摻雜濃度(10^{14} to 10^{18} cm^{-3})。另外，也可以延伸應用到 500MPa 單軸拉應力下。

The Error of Matthiessen's Rule in MOSFET electron Universal Mobility and Its Correction

Student: Yi-Hui Huang Advisor: Dr. Ming-Jer Chen

Department of Electronics Engineering and Institute of Electronics

National Chiao Tung University

Abstract

An analysis of the errors caused by Matthiessen's rule between the apparent universal mobility which is calculated by Matthiessen's rule and the simulated universal mobility curves are presented in this thesis. To focus on the high surface field region, the universal mobility features two distinct scattering mechanisms: one of phonon alone and one of surface roughness alone. By means of the experimentally-validated simulation package consisting of a self-consistent solving of Schrődinger and Poisson's equations and a universal mobility simulation program, we try to correct the experimental error of applying Matthiessen's rule to MOSFET mobility universality. Thus, the aim of this work is to devise an error-free version of Matthiessen's rule. The core of the new rule lies in a physically- based semi-empirical model, which explicitly expresses the errors due to the conventional use of Matthiessen's rule as a function of both the lowest subband population and the relative strength of individual mobility components. The new model holds under practical conditions (with temperatures up to 400 K) and in a broad range of substrate doping concentrations (10^{14} to 10^{18} cm^{-3}). Extension to the case of strain is also presented in terms of a uniaxial tensile stress of 500 MPa.

Acknowledgements

在碩士的求學中，我由另一間大學的研究所轉換到一個新環境，其實感到相當的恐懼與不安。非常感謝陳明哲教授在這些日子以來教導並指引我，讓我漸漸的熟識這個充滿溫暖的環境，並且在我遇到挫折時給予我方向，讓學生能夠得到勇氣努力地前進。此外，也相當的感謝博士班的李韋漢學長總是有耐心教導我，讓我得知自己的不足以及應該要努力的方向。感謝我們 309A 實驗室的學長、學姊、同學以及學弟妹們，謝謝你們陪伴我一同走過這些日子。另外還要再次感謝陳宛勵同學與葉婷衡同學，是你們讓我在這些奮鬥的日子裡多了一份歡樂，也學習到了許多事情。最後我要感謝一路上陪伴著我，為我擔心受怕的父母以及兄長，我有你們的支持才有勇氣走到這裡，並且努力認真地走下去，謝謝你們！

Contents

Figure Captions

Table Captions

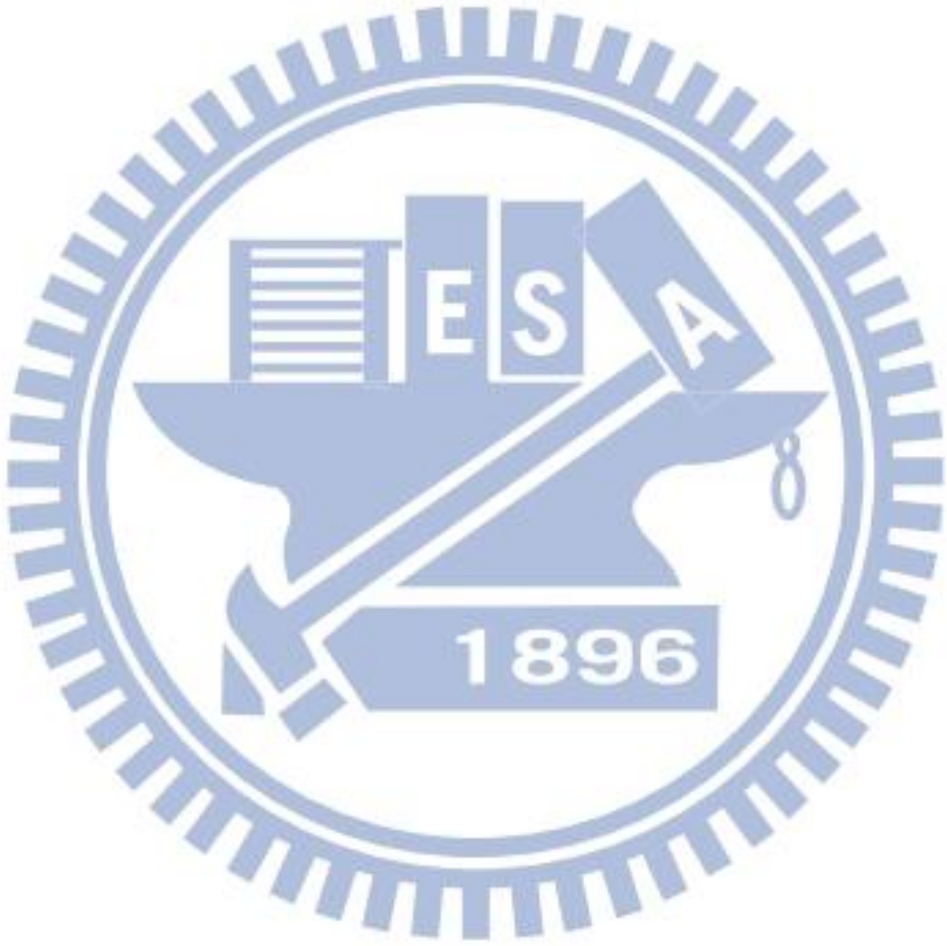

Chapter 1

Introduction

As we know, the mobility in the inversion layers of nMOSFETs can be limited to three primary scattering mechanisms: ones is the surface roughness scattering at SiO_2/Si substrate interface; second is the acoustic/optical phonon scattering in inversion channel region; and the final mechanism is the Coulomb impurity scattering due to the ionized impurity atoms in substrate depletion region.

Because of its additive property of reciprocal mobility components, Matthiessen's rule in principle may be a useful tool to probe individual scattering mechanisms in the inversion layers of nMOSFETs. It has been pointed out earlier by Stern [1] that the errors due to the use of Matthiessen's rule will be more than 15% for temperatures over 40K. Since then, there have been four fundamentally different methods concerning the validity and applicability of Matthiessen's rule [2]-[7] as published in the literature. First, Matthiessen's rule must be carried out under the extreme or impractical conditions such as very low temperatures (near absolute zero) [2]. Second, sophisticated numerical simulations on individual mobility components with no need to account for Matthiessen's rule [3] were used instead. Third, while assessing mobility components individually [4], [5], the errors caused by Matthiessen's rule were overlooked for the engineering purpose. Fourth, mobility simulations were performed to deliver the errors of mobility components extracted with the rule [3], [6], [7]. On the other hand, the current understanding of the error of Matthiessen's rule has been significantly improved.

In this thesis, we propose a new method in terms of an error-free version of Matthiessen's rule. This method is demonstrated in the universal mobility region and

takes the practical situations into account. The merit of the method is that it can correct the error of Matthiessen's rule and thereby ensure the applicability of the rule. Importantly, Stern [1] suggested the relative strength of individual mobility components as one origin of the errors. The other origin in terms of the subband population was put forward by Fischetti, et al. [3]. The establishment of the method in this work is closely linked to these two origins.

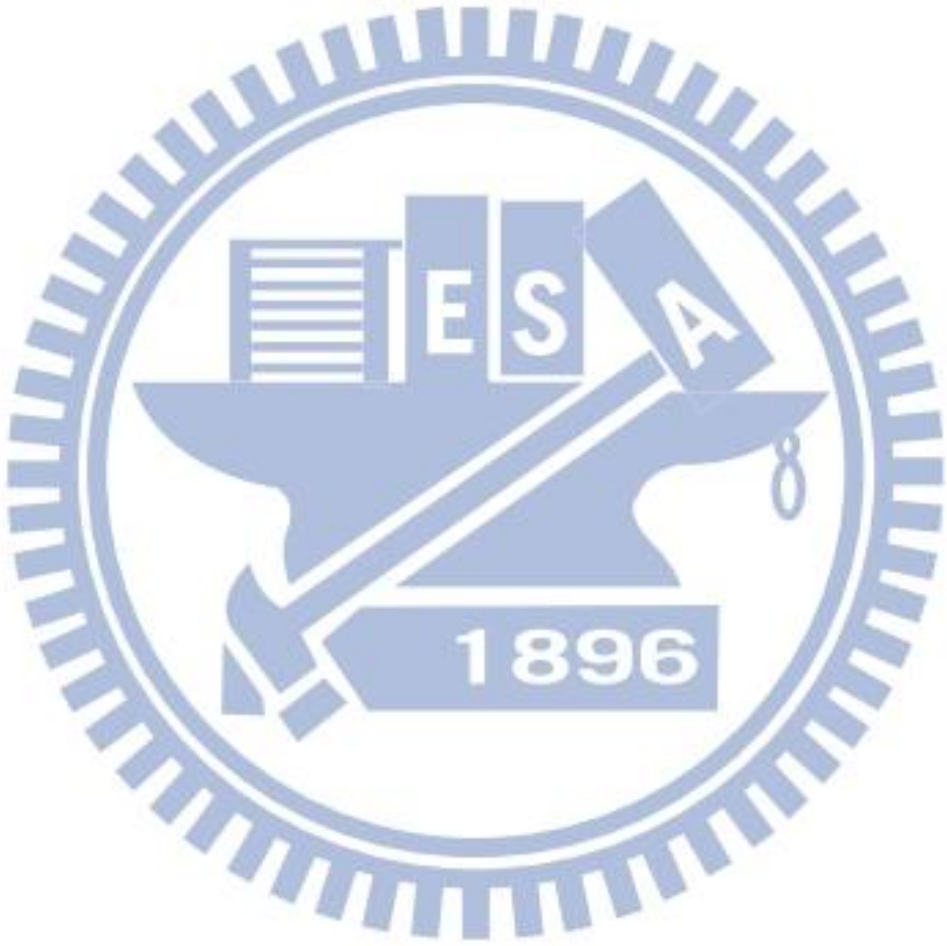

Chapter 2

Physical Theory for Quantum Simulator NEP

2.1 Schrődinger and Poisson Self-consistent "NEP" in n-MOSFETs

Self-consistent fully solving of Poisson and Schrődinger's equations in n-channel MOSFETs (metal-oxide-semiconductor field-effect transistors) [10] is introduced in terms of our Nano Electronics Physics **"NEP"** simulator.

The time-independent Schrödinger equation in the quantum mechanics can be expressed in terms of a matrix equation:

$$-\frac{\hbar^2}{2m}\nabla^2\Psi + V\Psi = E\Psi \tag{2.1}$$

Eq.(2.1) can be written as a general differential equation by the finite element method:

$$-\frac{\hbar^2}{2m}\left[\frac{\Psi(x_{i-1}) - 2\Psi(x_i) + \Psi(x_{i+1})}{\Delta x^2}\right] + V(x_i)\Psi(x_i) = E\Psi(x_i) \tag{2.2}$$

$$\Psi = \sum_n a_n \psi_n \tag{2.3}$$

where Ψ is the wave-function which be assumed that it is confined in a small region of W_q. Here W_q includes the entire inversion region. Generally, the wave-function Ψ dividing this region into n intervals of the equal-distance $\Delta x = W_q / n$ can be expanded by an orthogonal basis set $\{\psi_n\}$. Eventually, we solve the self-consistent Poisson and Schrődinger equations by Newton's method. Thus, the simulating results would contain the n eigen-values (E_n) corresponding to the n wave-function (ψ_n). The smallest eigen-value is defined as the ground state and the others are defined as the

excited states.

We give the schematic energy band diagram and physical environmental setup in Figure 2.1. The band diagram of silicon substrate along the out-of-plane direction is separated into two parts: one is the surface quantum confinement region ($W_{quantum}$) and the other is the bulk classical region ($W_{classical}$).

In the former region, the carriers are confined in this shallow region, where we meshed 300 intervals of width $dz_0 = 0.2$ nm to make sure the simulation accuracy. In the later region, we adopt the conventional formula; that is, ($W_{classical}$) is divided into 100 intervals with a width of $dz_1 = \frac{W_{classical}}{100}$. It can significantly reduce the computational time but not lose the accuracy. Additionally, the conduction band edge at the interface is set to be zero of energy in n-MOSFETs.

The common self-consistent step with the flowchart is illustrated in Figure 2.2. Firstly, we guessed the surface band bending V_s into the Poisson equation with the boundary conditions $V_{(z=0)} = V_s$ and $V_{(z=bulk)} = 0$. Then, it would obtain the corresponding initial potential profile $V(z)$, thus along with $V(z)$ to calculate 1D Schrődinger equation, as revealed in Eq.(2.1).

We can obtain the eigen-values and the wave-function as been mentioned in the previous paragraph. Moreover, we summarize the basic formulation and the iteration procedure we use to perform a self-consistent solution. In the surface quantum confinement region, the three-dimensional carriers in terms of electrons density $n_{3D}(z)$ and holes density $p_{3D}(z)$ can be described by

$$n_{3D}(z) = \sum_{i,j} \int_{E_{i,j}}^{\infty} DOS_{i,j}(E)_{2D}\, f(E) dE \cdot \left|\Psi_{i,j}(z)\right|^2$$

$$= \sum_{i,j} g_i \frac{m_{DOS}^i}{\pi\hbar^2} k_B T \ln\left(1+e^{(\frac{E_f - E_{i,j}}{kT})}\right) \cdot \left|\Psi_{i,j}(z)\right|^2 \tag{2.4}$$

$$p_{3D}(z) = \sum_{u,j} \int_{-\infty}^{E_{u,j}} DOS_{u,j}(E)_{2D}(1-f(E))dE \cdot \left|\Psi_{u,j}(z)\right|^2$$

$$= \sum_{u,j} g_u \frac{m_{DOS}^u}{\pi\hbar^2} k_B T \ln\left(1+e^{(\frac{E_{u,j} - E_f}{kT})}\right) \cdot \left|\Psi_{u,j}(z)\right|^2 \tag{2.5}$$

where *i* and *u* are the electron valley index and the hole valley index, respectively. *j* is the subband index, and g_i and g_u are the degeneracy of the *i*th valley and *u*th valley, respectively; m_{DOS}^i and m_{DOS}^u are the density of states electron and hole effective mass, and $E_{i,j}$ and $E_{u,j}$ are the electron and hole energy levels. The corresponding wave-functions $\Psi_{i,j}$ and $\Psi_{u,j}$ are all normalized. The carrier density in the bulk classical region is given by:

$$n(z) = N_C \cdot \frac{2}{\sqrt{\pi}} F_{1/2}\left(\frac{V(z)}{kT}\right) \tag{2.6}$$

$$p(z) = N_V \cdot \frac{2}{\sqrt{\pi}} F_{1/2}\left(\frac{-V(z)}{kT}\right) \tag{2.7}$$

where N_c and N_c are the conduction-band density of states and valence-band density of states, and $F_{1/2}$ is the Fermi-Dirac interal. Substituting these into the 1-D Poisson equation, we obtain

$$\frac{d^2V(z)}{dz} = -\frac{-e\cdot[-N_d^+(z) - n(z) + p(z)]}{\varepsilon_{si}} \tag{2.8}$$

where $N_d^+(z)$ is the ionized donor density. Ultimately, we can get a new potential $V(z)$ to satisfy Eq.(2.8) and use Newton's method to iterate the step continuously until the final potential profile $V(z)$ is obtained, within a tolerable error. The two-dimensional electron density can be described as

$$n_{i,j} = g_i \frac{m_{DOS}^i}{\pi\hbar^2} k_B T \ln\left(1+e^{\frac{E_f - E_{i,j}}{kT}}\right) \tag{2.9}$$

and the total inversion layer charge density is given as

$$N_{inv} = \sum_{i,j} n_{i,j} \tag{2.10}.$$

The average inversion layer thickness Z_{av} is written as

$$Z_{av} = \sum_{i,j}\left[\frac{n_{i,j}}{N_s} \cdot \int_0^{bulk} z \cdot \left|\Psi_{i,j}(z)\right|^2 dz\right] \tag{2.11}$$

The potential calculation for the high doping poly-silicon gate situation is demonstrated as:

$$V_{fb} = -k_B T \ln\left(\frac{N_{ploy} N_{sub}}{n_i^2}\right) \tag{2.12}$$

where V_{fb} is the flat band voltage, k_B is the Boltzmann's constant, N_{poly} is the poly gate concentration, N_{sub} is the substrate doping concentration and n_i is the intrinsic concentration. The poly gate voltage and oxide voltage are shown below:

$$V_{poly} = -\frac{\varepsilon_{Si} F_s^2}{2eN_{poly}} \tag{2.13}$$

$$V_{ox} = \frac{t_{ox}\varepsilon_{Si} F_s}{\varepsilon_{ox}} \tag{2.14}$$

where t_{ox} is the oxide thickness, ε_{si} and ε_{ox} are the dielectric constant of the silicon and oxide, respectively, and the surface electric field is given by $F_s = \frac{V_{(z=1)} - V_{(z=2)}}{\Delta z}$. Finally, the total gate voltage can be expressed as

$$V_g = V_s + V_{ox} + V_{poly} + V_{fb} \tag{2.15}$$

where V_s indicates the surface band bending determined by the potential profile in the silicon substrate.

Chapter 3

Electron Mobility Model

3.1 Introduction

In this section, we use the sub-band energy and the wave function provided by our NEP simulator to calculate the universal electron mobility under the relaxation time approximation. Then, we obtain corresponding mobility by only considering lowest four subbands in twofold valleys and two subbands in fourfold valleys.

In addition, we discussed the momentum relaxation rates caused by scattering with phonons and surface roughness which can be considered the expression of the universal mobility curve.

We also quoted the detailed model in a textbook by Lundstrom [9] to deal with the Coulomb scattering with ionized impurities in substrate of n-type polysilicon gate (n-polygate) to compare with the calculated ionized impurity mobility extracted by using Matthiessen's rule. Validity of Matthiessen's rule will be addressed in Chapter 4 as well. Figure 3.1 illustrates that the calculated universal electron mobility is insensitive to the substrate concentrations or process parameters when plotted as a function of high effective field (E_{eff}). In addition, E_{eff} can be defined via the empirical formula:

$$E_{eff} = \frac{e \cdot (\eta N_{inv} + N_{dep})}{\varepsilon_{si} \cdot \varepsilon_0} \tag{3.1.1}$$

where η is taken as 0.5. We determined the inversion carrier concentration (N_{inv}) and the surface concentration of the depletion charge (N_{dep}) by NEP. Eventually, all of the scattering parameters used in this work are listed on Table I.

3.2 Phonon Scattering Mechanism

As we all know, lattice vibrations will deform the crystal deformation potential, perturbing the dipole moment between atoms, and causing the degradation of inversion layer mobility due to the pressure waves which result from the lattice vibrations.

The mechanisms of phonon scattering can be classified into the acoustic phonon scattering and optical phonon scattering; acoustic phonon scattering displaces nearby atoms in the same directions and optical phonon scattering displaces adjacent atoms in opposite directions. Acoustic phonon energy is smaller than carrier energy while the k_{th} intervalley f-*type* phonon energy $E_{k(f)}$ is 59 meV, and the k_{th} intervalley g-*type* phonon energy $E_{k(g)}$ is 63meV according to the phase of the vibration with the two different atoms in one primitive cell.

Intravalley phonon scattering only considers acoustic phonons, thus according to Takagi, *et al.* [10], the momentum-relaxation rate $\tau_{ac}^{m,n}(E)$ from the m_{h} subband to the n_{th} subband is written as:

$$\frac{1}{\tau_{ac(2/4)}^{m,n}} = \frac{n_{v(2/4)}^{ac} m_{d(2/4)} \left(D_{ac}\right)^2 k_B T}{\hbar^3 \rho \left(s_l\right)^2} \frac{1}{W_{m,n}}, W_{m,n} = \left(\int \varphi_m^2(z)\varphi_n^2(z)dz\right)^{-1} \tag{3.2.1}$$

where the index of (2/4) in $\tau_{ac(2/4)}^{m,n}$ represents twofold valleys and fourfold valleys, respectively, n_{v2}^{ac} (=2)and n_{v4}^{ac} (=1) are the degeneracy of the twofold valleys and fourfold valleys with regard to intravalley scattering, respectively. D_{ac} (=13 eV) means the deformation potential due to acoustic phonons, ρ is the crystal density, s_l is the longitudinal sound velocity, $W_{m,n}$ is the form factor decided by the wave-functions of the m-th subband and the n-th subbands, which expresses the

interaction's effective thickness in the z-direction. It is the main difference of the 2D and 3D cases. k_B is the Boltzmann constant, and $\hbar$ is the Planck constant divided by 2π. The total scattering rate in the m_{th} subband is decided by summing up $\tau_{ac}^{m,n}$ within all the subbands where can be written as

$$\frac{1}{\tau_{ac(2/4)}^{m}(E)} = \sum_{n} \frac{U(E-E_m)}{\tau_{ac(2/4)}^{m,n}(E)} \tag{3.2.2}$$

where $U(x)\left(=1(x \geq 0)\ and\ 0(x<0)\right)$ is a step function.

For intervalley phonon scattering, the momentum-relaxation rate $\tau_{INTER}^{m,n}(E)$ from m_{th} subband in twofold valleys to the n_{th} subband in fourfold subband, according to Takagi, *et al.* [13], can be written as

$$\frac{1}{\tau_{INTER2}^{m,n}(E)} = \sum_{k}^{\{f\}} \frac{n_{n2\to4}^{f} m_{d4} \left(D_k\right)^2}{2\hbar\rho E_k} \frac{1}{W_{m,n}^{'}} \left(N_k + \frac{1}{2} \pm \frac{1}{2} \right) \times \frac{1-f(E \mp E_k)}{1-f(E)} \times U(E \mp E_k - E_n) \tag{3.2.3}$$

$$W_{m,n}^{'} = \left(\int \varphi_m^2(z) \varphi_n^{'2}(z) dz \right)^{-1} \tag{3.2.4}$$

where $n_{n2\to4}^{f}$(=4) indicates the degeneracy of the valleys for intervalley scattering, m_{d4} is density-of-states effective mass of the final state (fourfold valley), E_k and D_k are the deformation energy and potential for the k_{th} intervalley phonon. In addition, "+" means phonons emission and " — " means phonons absorption in the signs $\left(N_k + \frac{1}{2} \pm \frac{1}{2} \right)$, and N_k signifying the occupation number of the k_{th} intervalley phonon is defined as

$$N_k = \frac{1}{[\exp(\frac{E_k}{k_B T}) - 1]} \tag{3.2.5}$$

In the same way, the relaxation time $\tau_{INTER4}^{m,n}{}'(E)$ from m_{th} subband in fourfold valleys into the n_{th} subband in twofold subband, and $\tau_{INTER4}^{m,n}(E)$ from m_{th} subband in

fourfold valleys into the n_{th} subband in fourfold subband are described as

$$\frac{1}{\tau^{m,n}_{INTER4}{}'(E)} = \sum_{k}^{\{f\}} \frac{n^{f}_{n4\to 2} m_{d2} \left(D_k\right)^2}{2\hbar\rho E_k} \frac{1}{W_{m,n}} \left(N_k + \frac{1}{2} \pm \frac{1}{2} \right) \times \frac{1 - f(E \mp E_k)}{1 - f(E)} \times U(E \mp E_k - E_n^{'}) \quad (3.2.6)$$

$$\begin{aligned} \frac{1}{\tau^{m,n}_{INTER4}(E)} = & \sum_{k}^{\{f\}} \frac{n^{f}_{n4\to 4} m_{d4} \left(D_k\right)^2}{2\hbar\rho E_k} \frac{1}{W^{'}_{m,n}} \left(N_k + \frac{1}{2} \pm \frac{1}{2} \right) \times \frac{1 - f(E \mp E_k)}{1 - f(E)} \times U(E \mp E_k - E_n^{'}) \\ & + \sum_{k}^{\{g\}} \frac{n^{g}_{n4\to 4} m_{d4} \left(D_k\right)^2}{2\hbar\rho E_k} \frac{1}{W^{'}_{m,n}} \left(N_k + \frac{1}{2} \pm \frac{1}{2} \right) \times \frac{1 - f(E \mp E_k)}{1 - f(E)} \times U(E \mp E_k - E_n^{'}) \end{aligned} \quad (3.2.7)$$

$$W_{m,n} = \left(\int \varphi_m^{'\,2}(z) \varphi_n^2(z) dz \right)^{-1} \quad (3.2.8)$$

where $n^{f}_{n4\to 2}$(=2), $n^{g}_{n4\to 4}$(=1), and $n^{f}_{n4\to 4}$(=2) are the degeneracy of the intervalley phonon scattering, respectively.

3.3 Surface Roughness Scattering Mechanism

The roughness scattering at the interface of Si/SiO_2 is very important for a MOSFET device at high fields, resulting in the degradation of mobility in the inversion layer. There are usually two kinds of assumptions involved in the analysis of mobility, one is the exponential autocovariance function and the other is Gaussian autocovariance function.

We prefer using the Gaussian autocovariance function in this work because the surface roughness scattering rate calculated by exponential model needs larger values of the root mean square amplitude Δ to fit the mobility data of experimental than the Gaussian model.

Moreover, we need to make an important assumption that the approximation of single subband is quite accurate. We only consider the intrasubband scattering although surface roughness is anisotropic scattering. Due to Yamakawa, et al.'s surface roughness model [11] , the scattering rate for a Gaussian function is described

as

$$\frac{1}{\tau_{SR}^{i,j}(E)} = U(E-E_j)\frac{m_{DOS}^{(j)}(E)e^2 E_{eff}^{ij\ 2}\Delta^2\lambda^2}{2\hbar^3}\int_0^{2\pi} e^{\frac{-q^2\lambda^2}{4}}(1-\cos\theta)d\theta \tag{3.3.1}$$

Assuming the elastic collisions without energy transition, Eq. (3.3.1) can be rewrite as

$$\frac{1}{\tau_{SR}^{i,j}(E)} = U(E-E_j)\frac{m_{DOS}^{(j)}(E)e^2 E_{eff}^{ij\ 2}\Delta^2\lambda^2}{2\hbar^3}\int_0^{2\pi} 2\sin^2\frac{\theta}{2} e^{-\frac{2m(E-E_j)\lambda^2}{\hbar^2}\sin^2\frac{\theta}{2}}d\theta \tag{3.3.2}$$

$$q^2 = 2k^2(1-\cos\theta) = 4k^2\sin^2\frac{\theta}{2} \tag{3.3.3}$$

$$k^2 = \frac{2m_{DOS}^{(j)}\cdot(\mathrm{E}\text{-}\mathrm{E}_j)}{\hbar^2} \tag{3.3.4}$$

where $m_{DOS}^{(j)}$ and $\mathrm{E_j}$ are the density of states effective mass and the electron subband energy in the j_{th} subband, and λ is the correlation length. In addition, in order to obtain universal mobility curves more accurately, E_{eff}^{ij} can be presented by a new definition [11] in place of the empirical formula via Eq.(3.1.1). The compared results are described in Figure 3.2. The new definition of E_{eff}^{ij} is given as

$$E_{eff}^{ij} = \int_0^{\infty}\varphi^j(z)\frac{dV}{dz}\varphi^i(z)dz \tag{3.3.5}$$

where E_{eff}^{ij} is the electron effective field from the i_{th} subband to the j_{th} subband, $\varphi^i(z)$ and $\varphi^j(z)$ are the wave-functions of the initial and final states of the electrons, respectively.

3.4 Derivation of Two-Dimensional Mobility in the Universal Mobility Region

In this work, we can express the total scattering rates of the twofold and fourfold valley in terms of the phonon scattering and surface roughness scattering for i_{th} subband with the energy (E) as [10]:

$$\frac{1}{\tau_2^i(E)} = \frac{1}{\tau_{phonon2}^i(E)} + \frac{1}{\tau_{SR2}^i(E)} \tag{3.4.1}$$

$$\frac{1}{\tau_4^i(E)} = \frac{1}{\tau_{phonon4}^i(E)} + \frac{1}{\tau_{SR4}^i(E)} \tag{3.4.2}$$

for i_{th} subband of twofold and fourfold valleys, respectively. Then, the electron mobility μ_2^i and μ_4^i in i_{th} subband of twofold and fourfold valleys by using the average energy within the 2DEG in the relaxation time approximation can be given as

$$\mu_2^i = \frac{q_0 \int_{E_i}^{\infty} (E - E_i)\tau_2^i(E)(-\frac{\partial f}{\partial E})dE}{m_{c2} \int_{E_i}^{\infty} (E - E_i)(-\frac{\partial f}{\partial E})dE} \tag{3.4.3}$$

$$\mu_4^i = \frac{e \int_{E_i'}^{\infty} (E - E_i')\tau_4^i(E)(-\frac{\partial f}{\partial E})dE}{m_{c4} \int_{E_i}^{\infty} (E - E_i')(-\frac{\partial f}{\partial E})dE} \tag{3.4.4}$$

where m_{c2} and m_{c4} are the conductivity effective masses in two- and fourfold valleys, respectively. f is Fermi-Dirac distribution function. Eventually, we averaged over the subband occupation to obtain total universal mobility μ_{uni}, as described by

$$\mu_{uni} = \frac{(\sum_i \mu_2^i N_i + \sum_{i'} \mu_4^{i'} N_{i'})}{N_s} \tag{3.4.5}$$

3.5 Coulomb Scattering Mobility Model with Ionized Impurities in Substrate Region

The Coulomb scattering due to ionized impurity atoms in the substrate region results in the degradation of mobility at lower field. In this section, we use an analytical model derived elsewhere [9] to calculate ionized impurity mobility. The perturbing potential is the screened Coulomb potential [9], [12], as

$$U_s = \frac{e^2}{4\pi\varepsilon_o\varepsilon_{si}r}\exp(-r/L_D) \tag{3.5.1}$$

$$L_D = \sqrt{\frac{\varepsilon_{si}\varepsilon_o k_B T}{e^2 n_0}} \tag{3.5.2}$$

where r is the distance from the scattering center, L_D is the Debye length. ε_o is the permittivity of free space , and ε_{si} is the permittivity of the semiconductor (Si). n_0 is the 3-D density of the mobile carrier.

Then the scattering rate of Coulomb scattering due to ionized impurity in 3-D case can be presented by

$$\frac{1}{\tau_{imp}(E)} = \frac{N_I e^4}{16\sqrt{2m}\pi\varepsilon_o^2\varepsilon_{si}^2}[\ln(1+r^2) - \frac{r^2}{1+r^2}]E^{-\frac{3}{2}} \tag{3.5.3}$$

$$r^2 = 4L_D^2(\frac{p}{\hbar})^2 = \frac{8mEL_D^2}{\hbar^2} \tag{3.5.4}$$

where N_I is the ionized impurity concentration, However, Eq.(3.5.3) is not the 2-D electron gas inside the MOSFET, and our simulator is used for the two-dimensional inversion layers, thus the scattering rate of Coulomb scattering due to ionized impurity should be given in 2-D case.

According to [13], the momentum conservation in the z-direction of the

three-dimensional case at the scattering process of 2-D carriers should be replaced by the integral as

$$H_{2D}^2 = \int H_{3D}^2 \left| I(q_z) \right|^2 dq_z \tag{3.5.5}$$

$$I(q_z) = I_{mn}(q_z) \equiv \int \varphi_m(z) \varphi_n(z) e^{iq_z z} dz \tag{3.5.6}$$

where H_{2D} and H_{3D} are the matrix elements for two dimensions and three dimensions scattering, respectively. However, $|I_{mn}|^2$ is the form factor given by the wave-functions of the m-th subband and the n-th subbands, and it can be written as $W_{m,n}^{-1}$ which have be mentioned in section 3.2. Therefore, the scattering rate of ionized impurity scattering in 2-D case from m_{th} subband to n_{th} subband can be expressed as

$$\frac{1}{\tau_{imp,\Delta 2/4}^{m,n}(E)} = \frac{N_I e^4}{16\sqrt{2m}\pi\varepsilon_o^2\varepsilon_{si}^2}[\ln(1+r^2) - \frac{r^2}{1+r^2}]E^{-\frac{3}{2}} \frac{g_{2D}(E)}{g_{3D}(E)} \frac{1}{W_{m,n}} \tag{3.5.7}$$

where $g_{2D}(E)$ and $g_{3D}(E)$ are the density of states for two dimensions and three dimensions scattering, respectively. It should be noticed that only intrasubband scattering is considered.

According to [12], we let the Debye length of Eq.(3.5.2) to be rewritten as

$$L_D = \sqrt{\frac{\varepsilon_0 \varepsilon_{ox} Z_{av} k_B T}{e^2 N_{inv}}} \tag{3.5.8}$$

where N_{inv} and Z_{av} are the average 2-D inversion charge density and thickness of inversion layer which have be mentioned in Section.2.1 and can be calculated by NEP simulator.

Besides, the calculated total electron mobility including the influence on ionized impurity scattering mechanisms can be treated as mentioned in section 3.4. The total

scattering rates of the twofold and fourfold valley in terms of the phonon scattering, surface roughness scattering and ionized impurity scattering for i_{th} subband with the energy (E) can be described as [10]:

$$\frac{1}{\tau_2^i(E)} = < \frac{1}{\tau_{phonon2}^i(E)} + \frac{1}{\tau_{SR2}^i(E)} + \frac{1}{\tau_{imp2}^i(E)} > \tag{3.5.9}$$

$$\frac{1}{\tau_4^i(E)} = < \frac{1}{\tau_{phonon4}^i(E)} + \frac{1}{\tau_{SR4}^i(E)} + \frac{1}{\tau_{imp4}^i(E)} > \tag{3.5.10}$$

for i_{th} subband of twofold and fourfold valleys, respectively. And the electron mobility μ_2^i and μ_4^i in i_{th} subband of twofold and fourfold valleys can be defined as

$$\mu_2^i = \frac{e\int_{E_i}^{\infty} (E - E_i)\tau_2^i(E)(-\frac{\partial f}{\partial E})dE}{m_{c2}\int_{E_i}^{\infty} (E - E_i)(-\frac{\partial f}{\partial E})dE} \tag{3.5.11}$$

$$\mu_4^i = \frac{e\int_{E_i^{'}}^{\infty} (E - E_i^{'})\tau_4^i(E)(-\frac{\partial f}{\partial E})dE}{m_{c4}\int_{E_i}^{\infty} (E - E_i^{'})(-\frac{\partial f}{\partial E})dE} \tag{3.5.12}$$

Finally, we can acquire the total universal mobility μ_{tot} containing the influence on ionized impurity scattering mechanisms by the averaging over the subband occupation as

$$\mu_{tot} = \frac{(\sum_i \mu_2^i N_i + \sum_{i'} \mu_4^{i'} N_{i'})}{N_s} \tag{3.5.13}$$

3.6 The Effective Electron Mobility Calculated by Matthiessen's Rule

While comparing with universal mobility (μ_{uni}) at high electric field by using

our simulator, $\mu_{uni,M}$ is the apparent universal mobility in combination with phonon mobility and surface roughness mobility at high field. It can be defined based on Matthiessen's rule as follows:

$$\frac{1}{\mu_{uni,M}} = < \frac{1}{\mu_{ph}} > + < \frac{1}{\mu_{sr}} > \tag{3.6.1}$$

Besides, $\mu_{tot,M}$ is the total mobility which is constructed by phonon mobility, surface roughness mobility, and ionized impurity mobility according to Matthiessen's rule:

$$\frac{1}{\mu_{tot,M}} = < \frac{1}{\mu_{ph}} > + < \frac{1}{\mu_{sr}} > + < \frac{1}{\mu_{imp}} > \tag{3.6.2}$$

Besides, $\mu_{imp,M}$ is the mobility for ionized impurity mobility mechanism extracted with Matthiessen rule, as given by

$$\frac{1}{\mu_{imp,M}} = \frac{1}{\mu_{tot}} - \frac{1}{\mu_{uni}} \tag{3.6.3}$$

Refer to D.Esseni, *et al.*[5], we can compare $\mu_{imp,M}$ and μ_{imp} by the error $E_{r,imp}$ produced by Matthiessen's rule as

$$E_{r,imp} = \frac{\mu_{imp,M} - \mu_{imp}}{\mu_{imp}} \tag{3.6.4}$$

Figure 3.3 shows $\mu_{imp,M}$ and μ_{imp} for an inversion density $N_{inv} = 10^{12} cm^{-2}$ versus different substrate doping concentrations at 300 K. As we can see, the values of corresponding mobility are close to the simulation results of D.Esseni, *et al.*[5]. Besides, the error $E_{r,imp}$ which be defined in Eq. (3.6.4) calculated with six different substrate concentrations (10^{15} to 10^{18} cm^{-3}) versus inversion layer concentration are shown in Figure 3.4. Eventually, the resulting error $E_{r,imp}$ versus substrate doping concentration N_{sub} for an inversion density $N_{inv} = 10^{12} cm^{-2}$ is presented in

Figure 3.5, and the outcomes conform to Fig. 3 of [5] well. As shown, we can observe a discrepancy between $\mu_{imp,M}$ and μ_{imp}. This error is quite large. It is demonstrated that ionized impurity mobility extracted by Matthiessen's rule should not be regarded as experimental data.

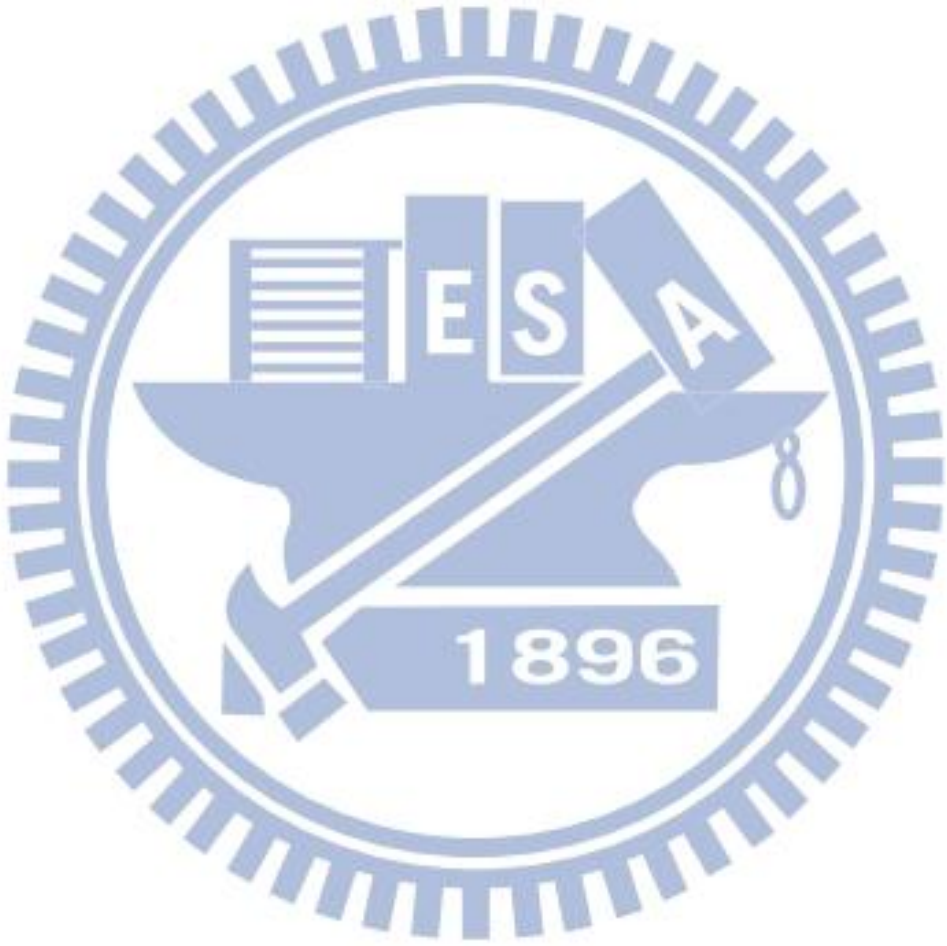

Chapter 4

Result and Discussion

4.1 Introduction

In this section, the resulting total mobility, consisting of phonon limited mobility, surface roughness limited mobility, and ionized impurity mobility, was found to reproduce experimental data [10] well for different substrate concentrations and different temperatures (T=397K, 342K, 242K, 297K). This was obtained for root mean square height of the surface roughness amplitude (Δ) of 2.9 Å and a correlation length of the surface roughness (λ) of 14.9 Å , which are mentioned in section 3.3. The result is also compared with Takagi et al.[10] as depicted in Figure 4.1. It can be seen that the larger the substrate doping concentration N_{sub}, the narrower the range of the vertical effective electric field *Eeff* dominated by phonon and surface roughness scatterings.

The validity of Matthiessen's rule has been known to be not exact for a long time. In this work, we show that the mobility extraction by using Matthiessen's rule would overestimate the value of experimental data. What's more, we analyze the accuracy of Matthiessen's rule and propose a simplified model for errors, finding the relationship with the errors between different substrate doping concentrations.

4.2 Model of the Error Produced by Matthiessen's Rule

Using the aforementioned parameters, the apparent universal mobility ($\mu_{uni,M}$) calculated by Matthiessen's rule, the simulated universal curves (μ_{uni}), phonon

limited mobility, surface roughness limited mobility and the errors E_r between $\mu_{uni,M}$ and μ_{uni} versus E_{eff} are plotted in Figure 4.2 for N_{sub}=10^{18} cm^{-3} at 300K. The inset in Figure 4.2 shows the corresponding population of two lowest subbands. The errors E_r between $\mu_{uni,M}$ and μ_{uni} can be defined as

$$E_r = \frac{\mu_{uni,M} - \mu_{uni}}{\mu_{uni}} \tag{4.2.1}$$

However, we calculated the universal mobility and the corresponding error quantitatively by the compared method are given below,

$$\frac{1}{\mu_{uni}} = < \frac{1}{\mu_{phonon}} + \frac{1}{\mu_{SR}} > \tag{4.2.2}$$

where $\mu_{uni,M}$ have been defined in Eq. (3.6.1).

Remarkably, we found that the largest errors occur at a critical E_{eff} where phonon limited mobility is equal to surface roughness limited mobility and apart from this point the errors decrease gradually, as shown in Figure 4.2. This indicates the relative strength of phonon limited and surface roughness limited mobility [1]. The population of subband i of valley j can be defined as p^{ij}, and come from the other origin [3], the twofold lowest subband population p_o which also be described as p^{11} can be drawn under $\mu_{ph} = \mu_{sr}$ as shown in the inset of Figure 4.2.

The comparison results with other substrate doping concentrations (10^{14} to 10^{17} cm^{-3}) and different temperatures (100 to 300K) are shown in Figure 4.3 to Figure 4.5. These figures pointed out that Matthiessen's rule overestimates the extracted universal mobility. Specifically, the maximum error of universal mobility caused by using Matthiessen's rule is below 30%.

Note that the critical E_{eff} is larger than 1 MV/cm in Figure 4.2 and far away from the Coulomb scattering region due to ionized impurity as experimentally shown in Figure 4.6.

A scatter plot between the peak of error $E_{r,max}$ and the corresponding twofold lowest subband population p_o (under $\mu_{ph}=\mu_{sr}$) for different substrate doping concentrations (10^{14} to 10^{18} cm^{-3}) with temperature as a parameter is shown in Figure 4.7. Because the separation of subband is strong with high doping concentration, more inversion carrier occupies on lowest subband with high doping concentration and low temperature. We found that the peak of error $E_{r,max}$ increase for increasing temperatures and decreasing substrate doping concentrations. Obviously, there is a unique relationship existing. We can figure out a power-law relationship between the two:

$$E_{r,\max} = ap_o^{\gamma} \tag{4.2.3}$$

where a is the pre-factor and γ is the power-law exponent. In Figure 4.8 we show different temperatures corresponding to different values of a, and different temperatures corresponding to different values of γ as depicted in Figure 4.9.

However, there is a fitting line that can be drawn in Figure 4.8 and Figure 4.9, yielding $a = -0.024 + 2.49\times10^{-4}$ T and $\gamma = 1/ (0.026 - 9\times10^{-4}$ T) in Figure 4.8 and Figure 4.9, respectively, regardless of the doping concentrations.

At this point, we are able to establish a semi-empirical model in the context of the relative strength of μ_{ph} and μ_{sr}:

$$E_r = E_{r,\max}(1-\alpha\exp(\beta\frac{\min(\mu_{ph},\mu_{sr})}{\max(\mu_{ph},\mu_{sr})})) \tag{4.2.4}$$

Through best fitting, we obtained β = -5 and α = 1 and 2 for $\mu_{ph} < \mu_{sr}$ and $\mu_{ph} > \mu_{sr}$, respectively. The validity of the error calculated by Eq.(4.2.3) and Eq.(4.2.4) has been confirmed by the simulation for different substrate doping concentrations (10^{14} to 10^{18} cm^{-3}) at 300 K. The left hand side of Figure 4.10 reveals

such results for five different substrate doping concentrations at 300 K as $\mu_{ph} < \mu_{sr}$, and the results for $\mu_{ph} > \mu_{sr}$ as shown in the right hand side of Figure 4.10. Note that under the critical situation of $\mu_{ph} = \mu_{sr}$, E_r in Eq. (4.2.4) reduces to its peak value $E_{r,max}$.

Finally, we want to highlight that the validity of the errors E_r between μ_{uni} and $\mu_{uni,M}$ which did not consider the mobility of ionized impurity at high E_{eff} region in this work is adequate. Therefore, we calculated the total mobility μ_{tot} consist of phonon limited mobility, surface roughness limited mobility, and ionized impurity mobility as

$$\frac{1}{\mu_{tot}} = < \frac{1}{\mu_{phonon}} + \frac{1}{\mu_{SR}} + \frac{1}{\mu_{IMP}} > \tag{4.2.5}$$

The corresponding error $E_{r,tot}$ of total mobility caused by using Matthiessen's rule is

$$E_{r,tot} = \frac{\mu_{tot,M} - \mu_{tot}}{\mu_{tot}} \tag{4.2.6}$$

where $\mu_{tot,M}$ have been mentioned in Eq. (3.6.2).

The results for five different substrate doping concentrations (10^{15} to 10^{18} cm^{-3}) at 300K are shown in Figure 4.11, and it has been mentioned in [6] that the error due to ionized impurity part is larger than phonon part. Figure 4.12 shows a scatter plot between the peak of error for E_{eff} larger than 1 MV/cm versus the corresponding twofold lowest subband population p_o (under $\mu_{ph}=\mu_{sr}$) for different substrate doping concentrations for comparison with result in Figure 4.6. The comparison results pointed out that although using universal curves (μ_{uni}) to calculate the error by Eq. (4.2.1) may influence the value of $E_{r,max}$, it is insignificant to compare the difference between the $E_{r,max}$ and the peak of $E_{r,tot.}$ Thus, the effect of ionized impurity mobility can be suppressed evidently in the high vertical electric field region. Therefore, the validity of the peak error in this work is adequate.

However, it should be noticed that the critical E_{eff} is smaller than 1 MV/cm when

temperature decreasing to 100K as shown in Figure 4.5. Because phonon limited mobility increase as temperature decreasing and surface roughness limited mobility is less dependent on temperature, the critical E_{eff} under $\mu_{ph} = \mu_s$ would move into low vertical electric field region, thus the effect of ionized impurity mobility should be considered.

4.3 Correction Model of Matthiessen's Rule

Based on the above analysis, we will show how to correct Matthiessen's rule in the high vertical effective electric field in this section. The error-free version of Matthiessen's rule is reached by combining Eq. (4.2.3) and Eq. (4.2.4):

$$\frac{1}{\mu_{uni}} = \left(\frac{1}{\mu_{ph}} + \frac{1}{\mu_{sr}}\right)(1 + E_r) \tag{4.3.1}$$

In executing this method, only the self-consistent solving of coupled Poisson equations and Schrödinger's equations is needed with aim to determine the critical E_{eff} under $\mu_{ph} = \mu_{sr}$, which in turn determines the peak of E_r, and hence the corresponding twofold lowest subband population p_o. Once p_o is known, we can readily determine the maximum error $E_{r,max}$ via Eq. (4.2.3). As a consequence, the E_r in Eq. (4.3.1) becomes a function of only the ratio of μ_{ph} and μ_{sr} according to Eq. (4.2.4). Therefore, we can directly obtain the universal mobility μ_{uni} for given μ_{ph} and μ_{sr} by using Eq.(4.2.4); otherwise, the value of universal mobility will be overestimated as in Figure 2.1 in terms of $\mu_{uni,M}$.

Reciprocally speaking, this method of Eq.(4.3.1) can work for μ_{ph} and μ_{sr} assessment for case of given universal mobility μ_{uni} data. To demonstrate this, one may quote the mobility extraction study by Takagi, *et al*. [4] and Hauser [5] in terms of their empirical models of μ_{ph} and μ_{sr}. Since these experimentally-determined

models were obtained based on the conventional use of Matthiessen's rule and according to Eq. (4.3.1), the resulting μ_{ph} and μ_{sr} are definitely underestimated and must be further multiplied by a factor of $(1 + E_r)$, as shown in Figure 3.3.

Finally, we want to stress that the proposed method can work for other situations like strain effect of mobilities. In Figure 4.13, we show a scatter plot of the peak E_r that is the maximum error $E_{r,max}$ and the twofold lowest subband population p_o, which were created via simulations for <110> uniaxial tensile stress of 500 MPa. Noticeably, the effect of strain is primarily to increase p_o. In this strain case, the power-law relationship Eq. (4.2.4) again holds, as depicted in this figure.

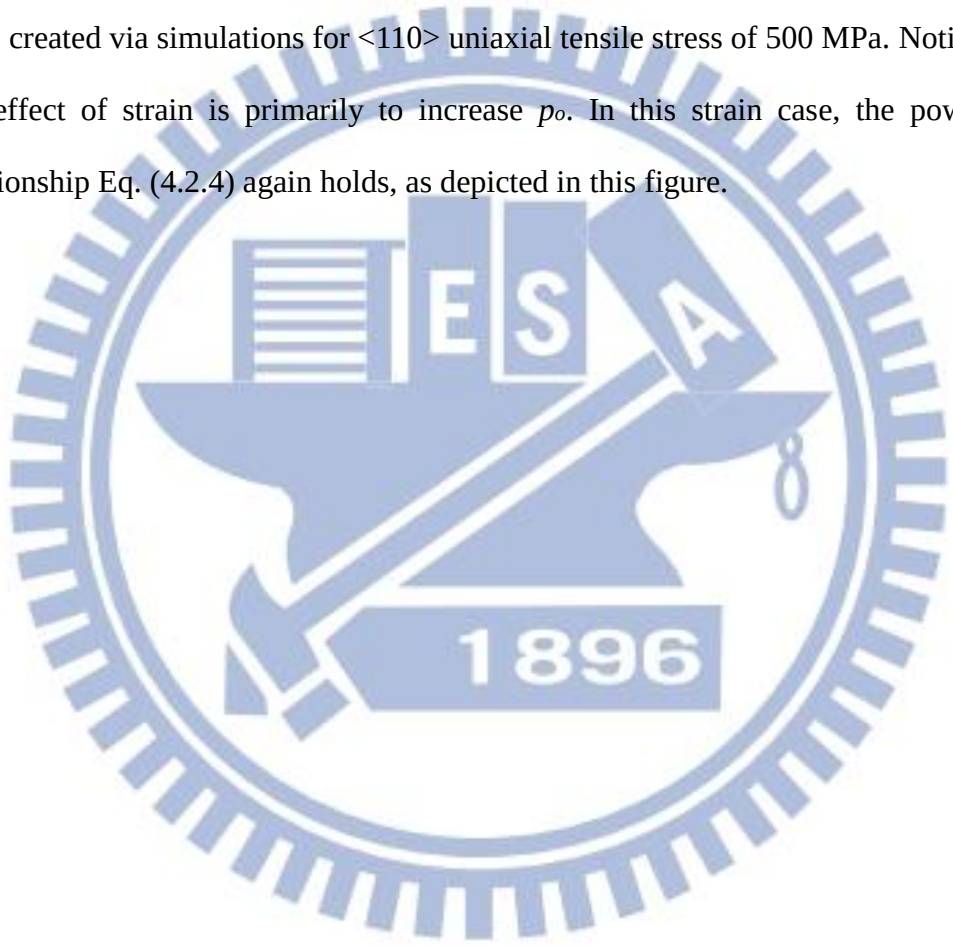

Chapter 5

Conclusion

In this work, we have shown that the universal mobility produced by Matthiessen's rule may not be considered as the result of experimental data, because the error between the universal mobility of simulations and the apparent universal mobility calculated by Matthiessen's rule is worse. It may even cause the wrong trends of mobility characterization.

We also quoted the detailed formula to calculate the Coulomb-limited mobility due to ionized impurity atoms in substrate region; the simulated result is comparable with D. Esseni, *et al* [6]. The extracted ionized impurity mobility by using Matthiessen's rule also exhibits a large discrepancy as compared with simulated one.

The analysis results in this thesis point out that overlooking the error of Matthiessen's rule only leads to poor extraction of individual mobility components. Therefore, through the experimentally-validated universal mobility simulation, a semi-empirical model for the errors of Matthiessen's rule has been established in this work. As a consequence, the conventional extraction error can be corrected using an error-free version of Matthiessen's rule which has been created in this thesis.

References

[1] F. Stern, “Calculated temperature dependence of mobility in silicon inversion layers,” *Phys. Rev., Lett.* , vol. 44, no. 22, pp. 1469-1472, Jun.1980.

[2] J. Li and T. P. Ma, “Scattering of silicon inversion layer electrons by metal/oxide interface roughness,” *J. Appl. Phys.*, vol. 62, no. 10, pp. 4212-4215, Nov. 1987.

[3] M. V. Fischetti, F. Gámiz, and W. Hänsch, “On the enhanced electron mobility in strained-silicon inversion layers,” *J. Appl. Phys.*, vol. 92, no. 12, pp. 7320-7324, Dec. 2002.

[4] S. Takagi, A. Toriumi, M. Iwase, and H. Tango, “On the universality of inversion layer mobility in Si MOSFET’s: Part I – Effects of substrate impurity concentration,” *IEEE Trans. Electron Devices*, vol. 41, no. 12, pp. 2357-2362, Dec. 1994.

[5] J. R. Hauser, “Extraction of experimental mobility data for MOS devices,” *IEEE Trans. Electron Devices*, vol. 43, no. 11, pp. 1981-1988, Nov. 1996.

[6] D. Esseni and F. Driussi, “A quantitative error analysis of the mobility extraction according to the Matthiessen rule in advanced MOS transistors,” *IEEE Trans. Electron Devices*, vol. 58, no. 8, pp. 2415-2422, Aug. 2011.

[7] M. J. Chen, S. C. Chang, S. J. Kuang, C. C. Lee, W. H. Lee, K. H. Cheng, and Y. H. Zhan, “Temperature-dependent remote-Coulomb-limited electron mobility in n+-polysilicon ultrathin gate oxide nMOSFETs,” *IEEE Trans. Electron Devices*, vol. 58, no. 4, pp. 1038-1044, Apr. 2011.

[8] A. M. Cruz Serra and H. Abreu Santos, “A one-dimensional, self-consistent numerical solution of Schrődinger and Poisson equations,” *J. Appl. Phys.*, vol. **70**, no. 5, pp. 2734-2738, Sep. 1991.

[9] L. Mark, *Fundamentals of carrier transport*, second edition, Cambridge Univ. Pr. ,

2009.

[10] S. Takagi, J. L. Hoyt, J. J. Welser, and J. F. Gibbons, “Comparative study of phonon-limited mobility of two-dimensional electrons in strained and unstrained Si metal-oxide-semiconductor field-effect transistors,” *J. Appl. Phys.*, vol. **80**, no. 3, p. 1567, Aug. 1996.

[11] S. Yamakawa, H. Ueno, K. Taniguchi, C. Hamaguchi, K. Miyatsuji, K. Masaki, and U. Ravaioli, “Study of interface roughness dependence of electron mobility in Si inversion layers using the Monte Carlo method,” *J. Appl. Phys.*, vol. 79, no. 2, pp. 911–916, Jan. 1996.

[12] P. Siddharth, G. Neil, and P. Gary,“A quasi-two-dimensional depth-dependent mobility model suitable for device simulation for Coulombic scattering due to interface trapped charges”, *Journal of Applied Physics* 100, 044516, 2006.

[13] K. Hirakawa and H. Sakaki, “Mobility of the two-dimensional electron gas at selectively doped n-type $Al_xGa_{1-x}As$/GaAs heterojunctions with controlled electron concentrations”, *Physical Review B*: Condensed Matter, 33, 8291-8303.

[14] D. K. Ferry, *Semiconductors* (Macmillan, New York, 1991).

[15] A. Pirovano, A. L. Lacaita, G. Ghidini, and G. Tallarida, “On the correlation between surface roughness and inversion layer mobility in Si-MOSFETs,” *IEEE Electron Device Lett.*, vol. **21**, no. 1, pp. 34–36, 367, Jan. 2000.

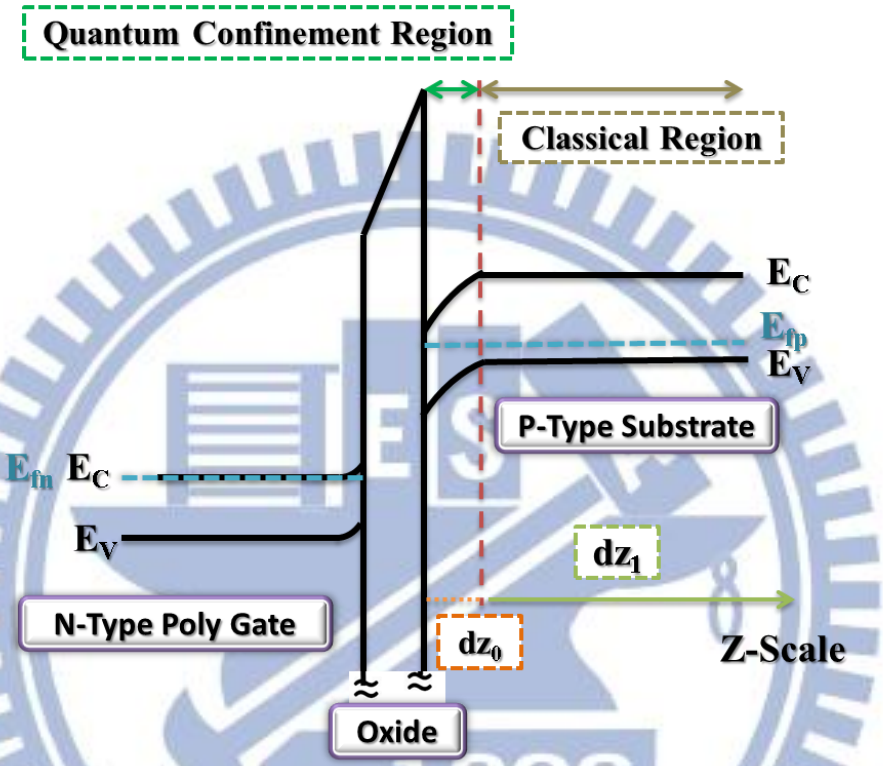

Figure 2.1 The energy band diagram of a poly gate/SiO_2/p-substrate system.

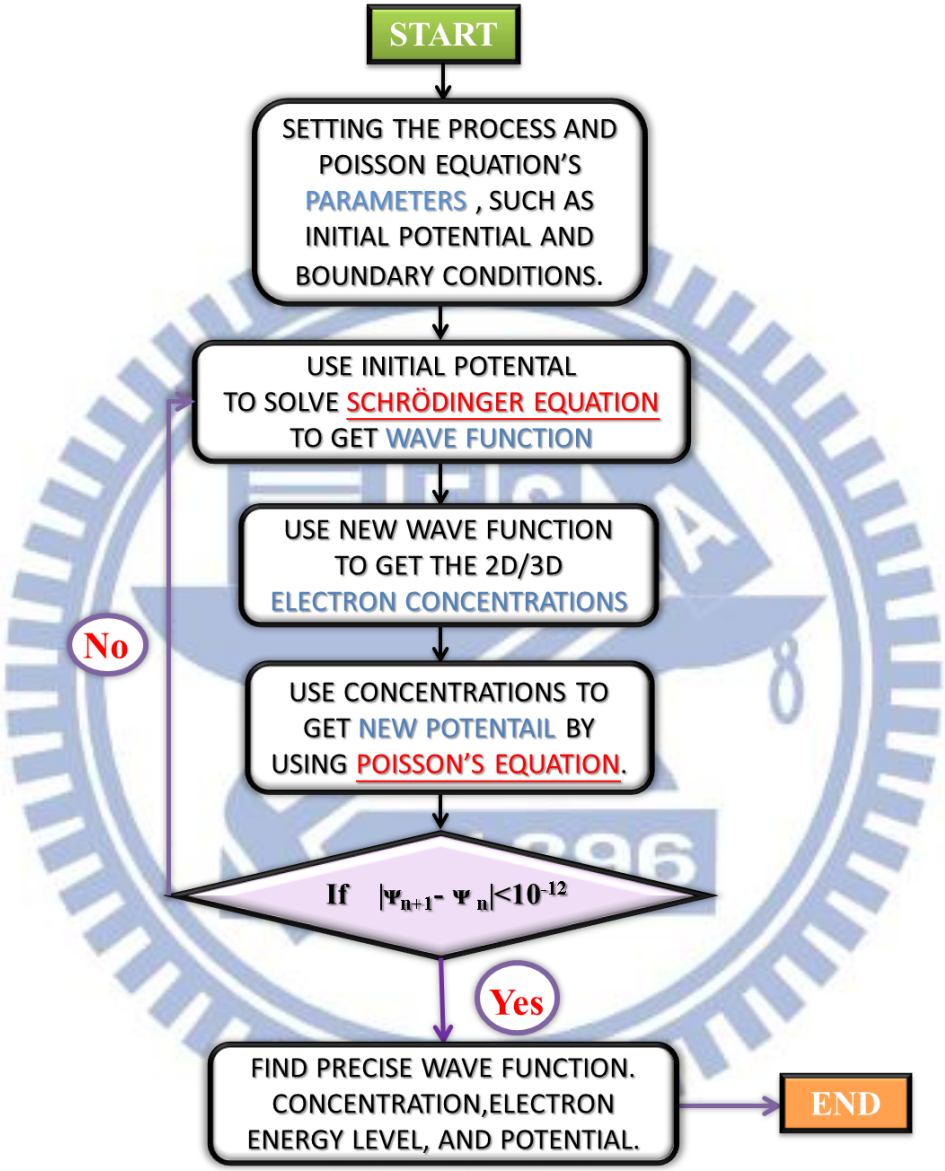

Figure 2.2 The flowchart of Poisson and Schrödinger self-consistent solving procedure.

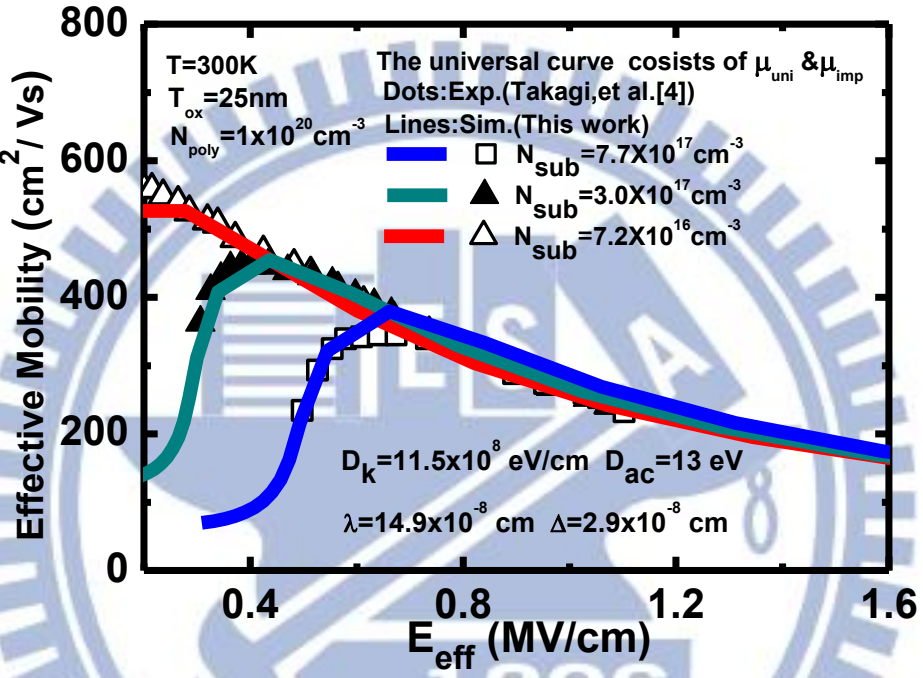

Figure 3.1 The simulated universal mobility (lines) versus vertical effective electric field with substrate doping concentration (N_{sub}) as a parameter. Experiment data [4] are sited for comparison.

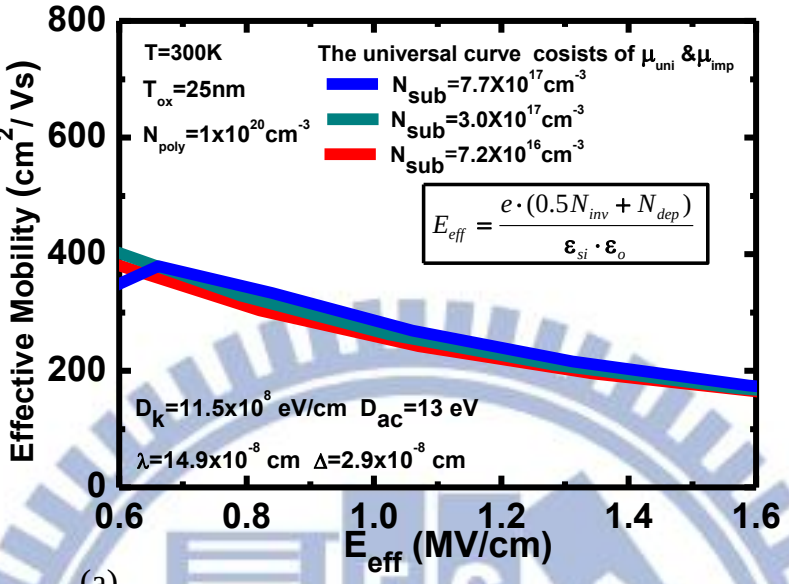

(a)

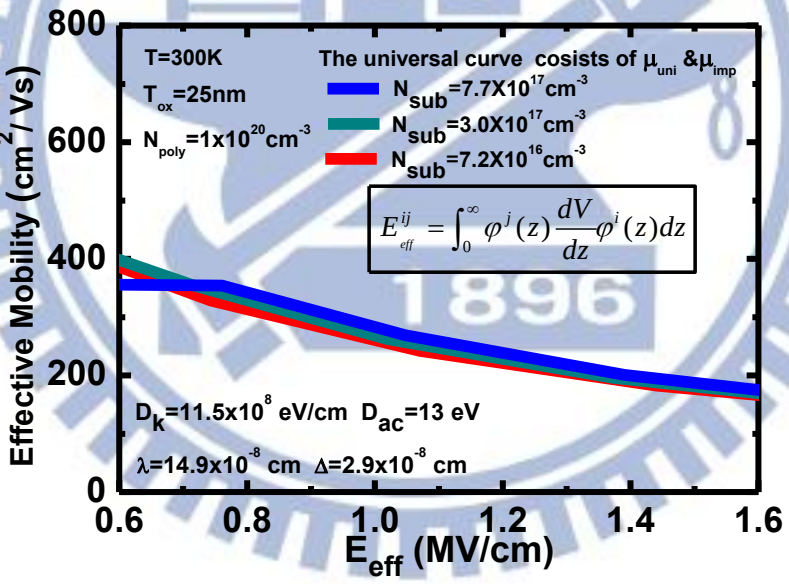

(b)

Figure 3.2 The simulated universal mobility (lines) with substrate doping concentration (N_{sub}) as a parameter in surface roughness model for two different defined of the electric field for (a) the experimentally empirical formula; and (b) the vertical electric field as defined in Eq.(3.1.1) of [11].

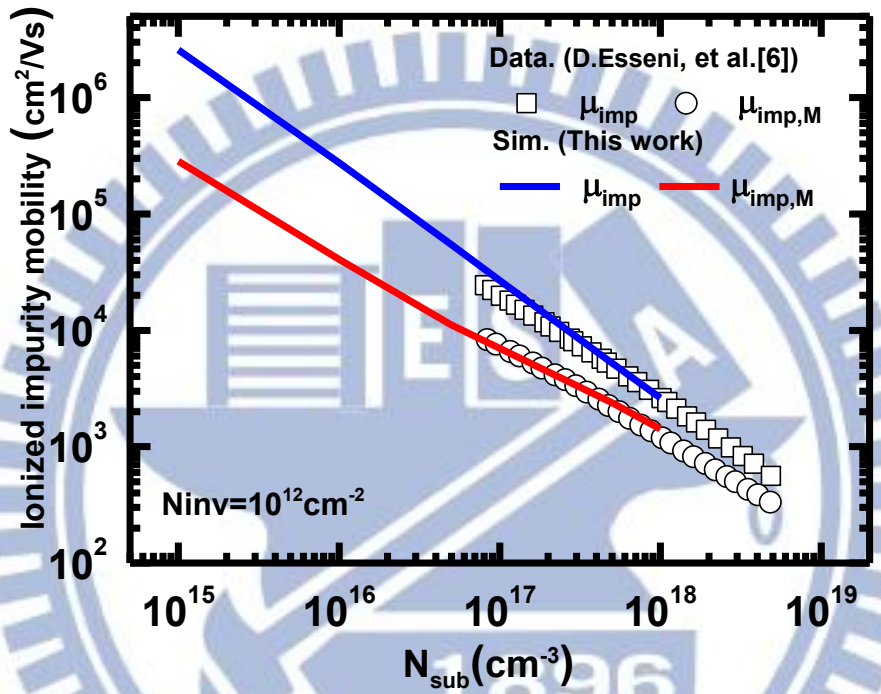

Figure 3.3 The comparison of the data (symbols) [6] and ionized impurity limited mobility curves from the simulated results (blue line) and the extracted results by Matthiessen's rule (red line) versus different substrate doping concentrations for an inversion layer $N_{inv}=10^{12}$ cm^{-2} at 300 K.

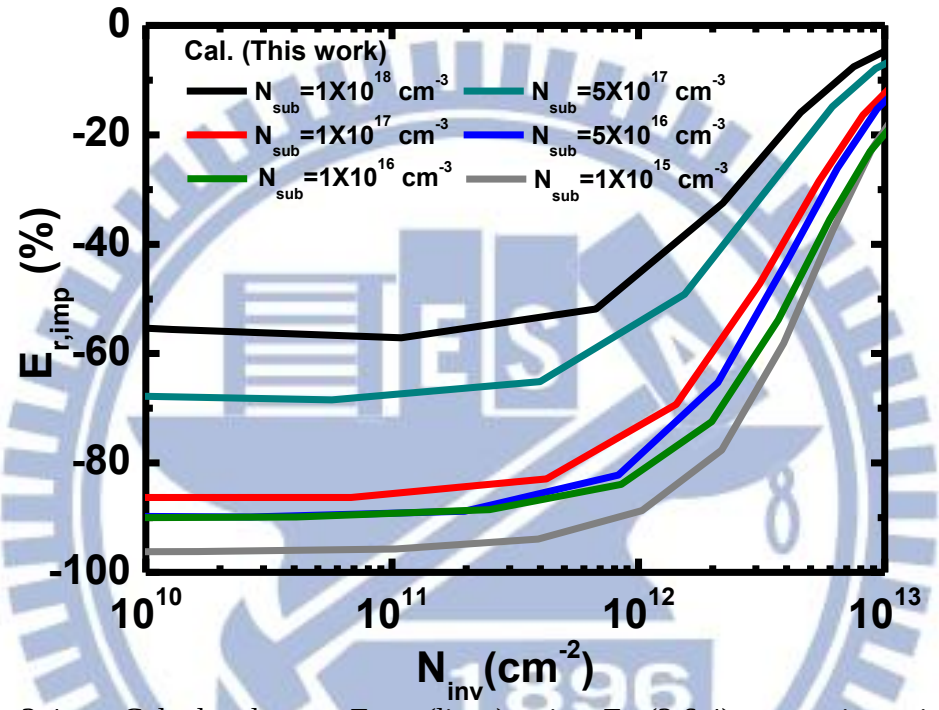

Figure 3.4 Calculated error $E_{r,imp}$ (lines) using Eq.(3.6.4) versus inversion layer concentration for six different substrate doping concentrations (10^{15} to 10^{18} cm^{-3}) at 300 K.

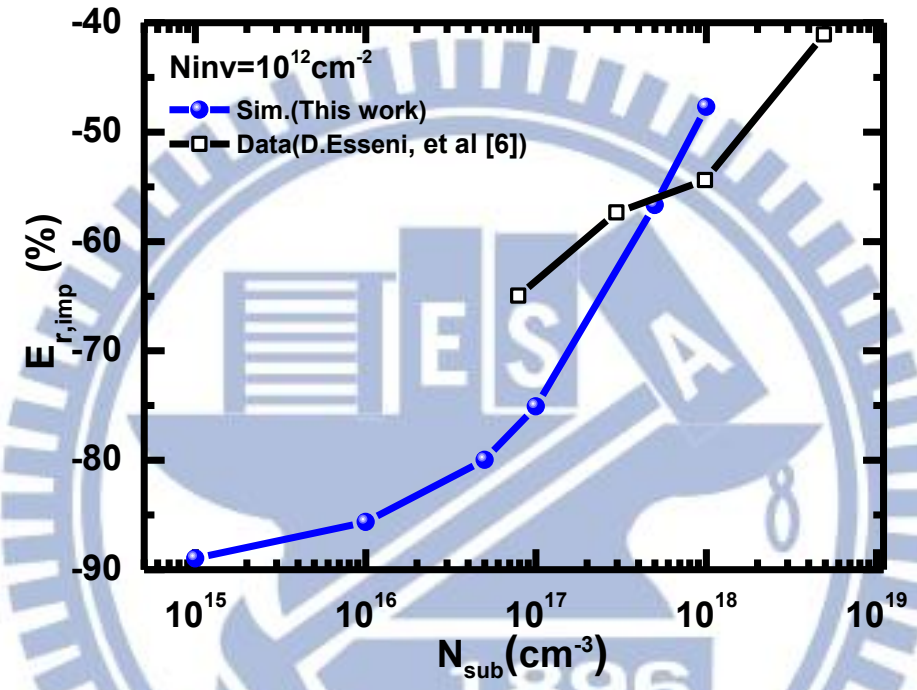

Figure 3.5 The error $E_{r,imp}$ calculated using Eq.(3.6.4) versus substrate doping concentration for an inversion density $N_{inv} = 10^{12} cm^{-2}$. Also plotted for comparison with the simulations from Fig. 3 of [6].

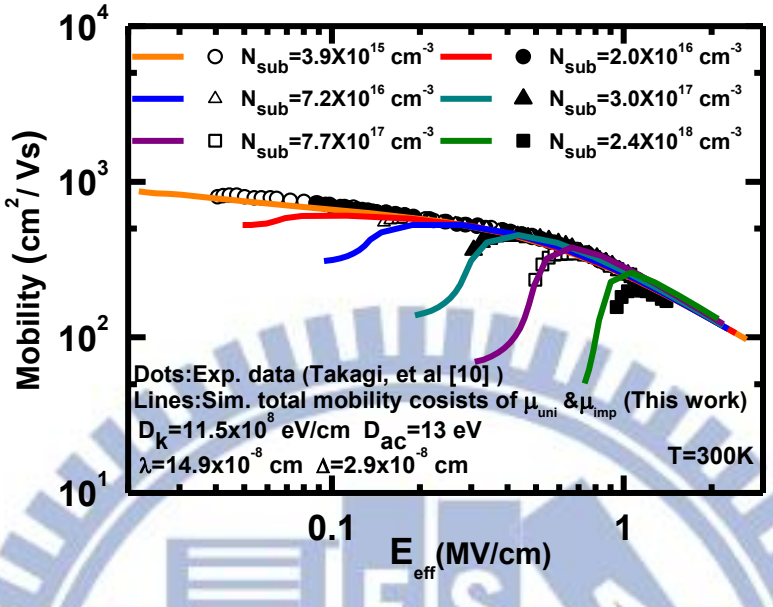

(a)

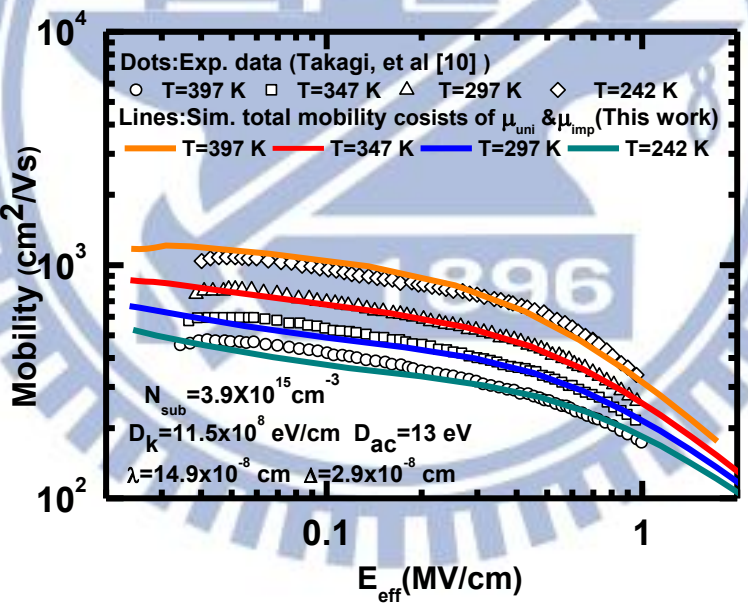

(b)

Figure 4.1 Comparison of simulated electron total mobility (lines) with the experimental one (symbols) [10] versus vertical effective electric field with Δ = 2.9 Å and λ =14.9 Å for (a) six substrate concentrations and (b) four temperatures of 397K, 342K, 242K, and 297K.

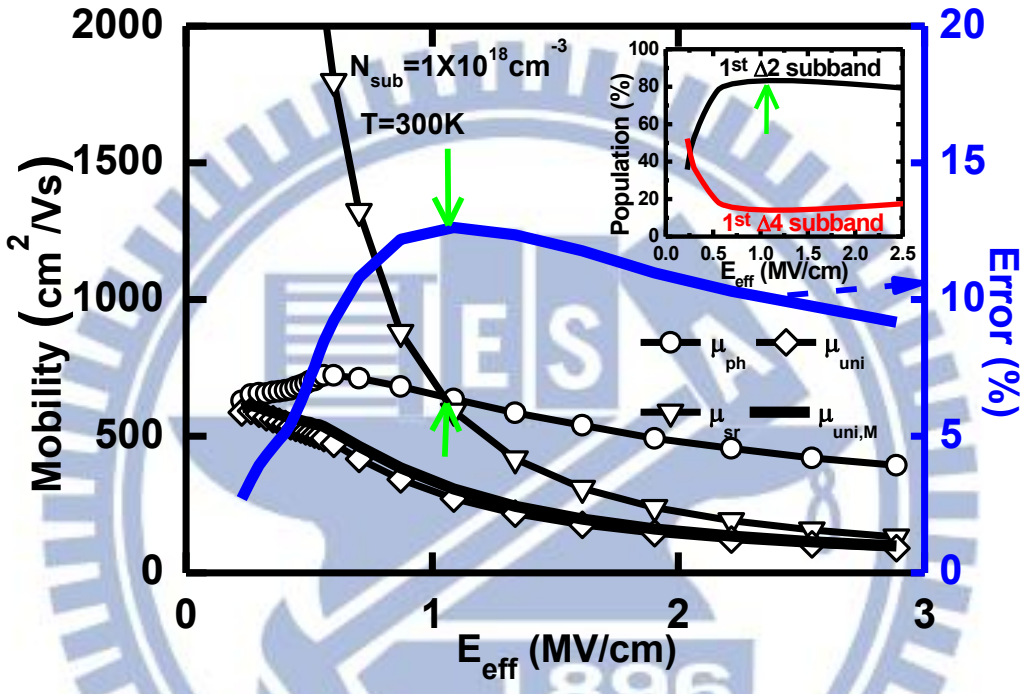

Figure 4.2 Simulated universal mobility, phonon limited mobility, and surface roughness limited mobility (lines with symbols) versus E_{eff} for N_{sub} = 10^{17} cm^{-3} at 300K. The apparent universal mobility (lines) obtained by Matthiessen's rule and hence the errors are together plotted. The arrow indicates the critical E_{eff} where phonon and surface roughness limited mobilities have the same value. The inset shows corresponding population of two lowest subbands.

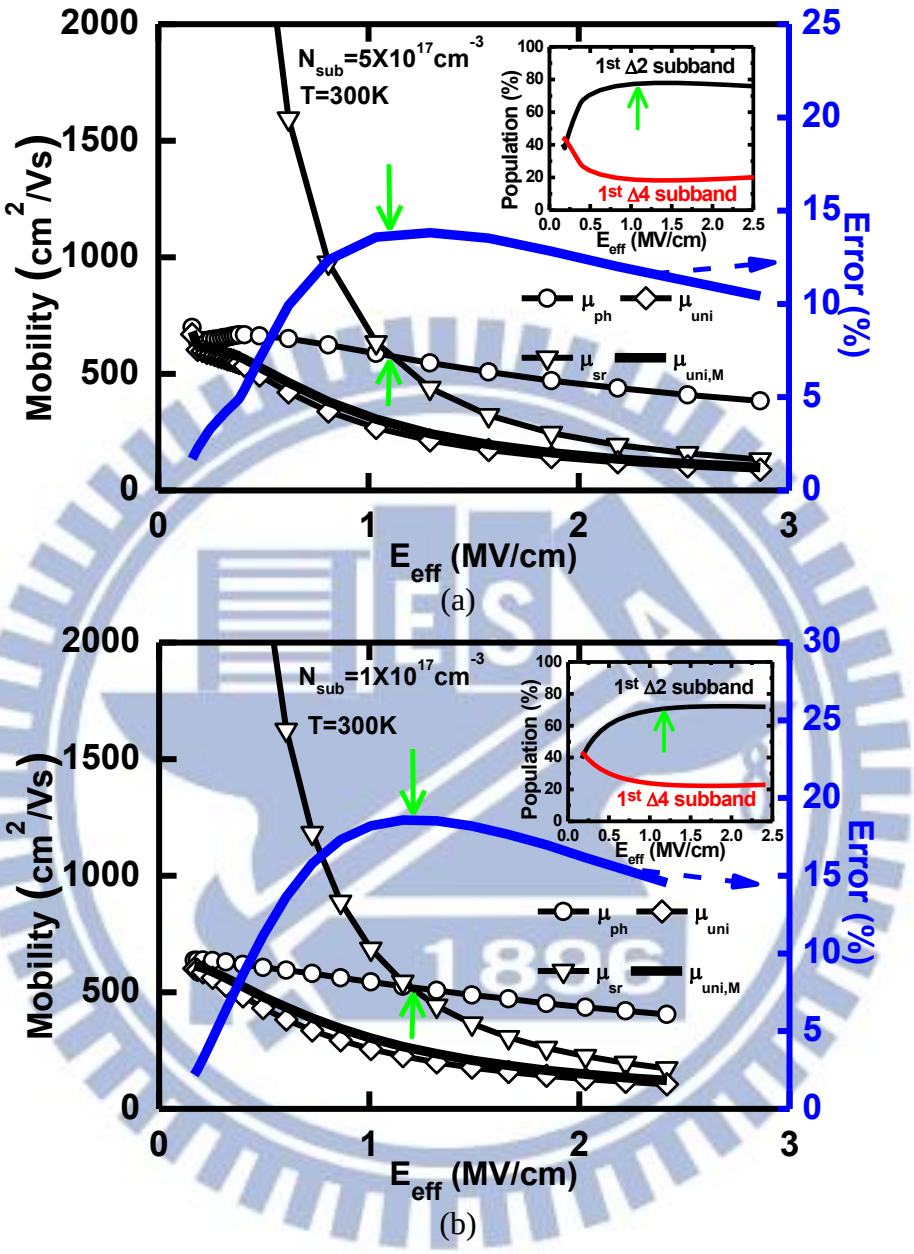

Figure 4.3 The apparent universal mobility (lines) obtained by Matthiessen's rule, simulated universal mobility, phonon limited mobility, and surface roughness limited mobility (lines with symbols) versus E_{eff} for (a) $N_{sub} = 5\times10^{17}$ cm^{-3}, (b) $N_{sub} = 10^{17}$ cm^{-3}, (c) $N_{sub} = 10^{16}$ cm^{-3}, (d) $N_{sub} = 10^{15}$ cm^{-3}, and (e) $N_{sub} = 10^{14}$ cm^{-3} at 300K. The arrow indicates the critical E_{eff} where phonon and surface roughness limited mobilities have the same value. The inset shows corresponding population of two lowest subbands.

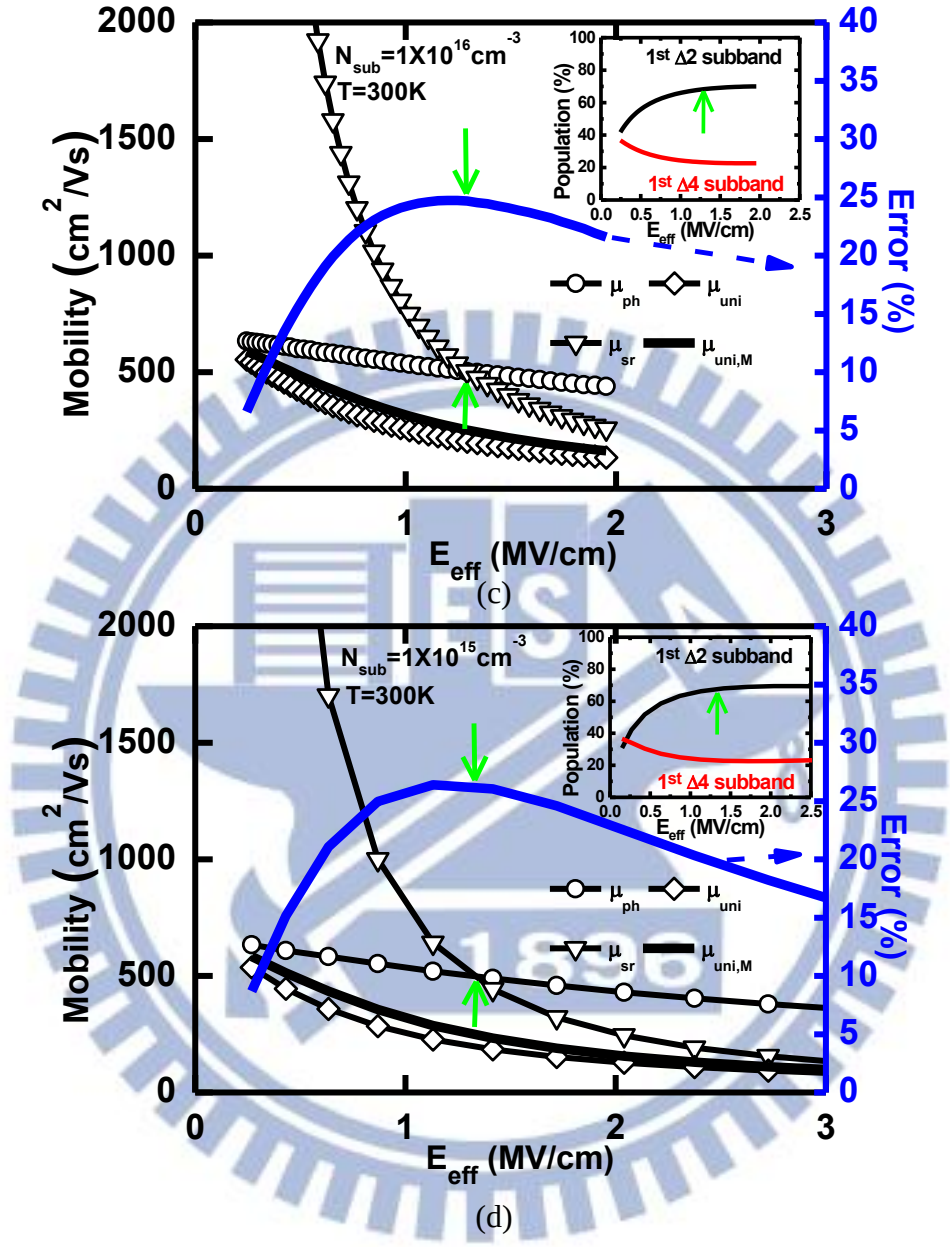

Figure 4.3 The apparent universal mobility (lines) obtained by Matthiessen's rule, simulated universal mobility, phonon limited mobility, and surface roughness limited mobility (lines with symbols) versus E_{eff} for (a) $N_{sub} = 5\times10^{17}$ cm^{-3}, (b) $N_{sub} = 10^{17}$ cm^{-3}, (c) $N_{sub} = 10^{16}$ cm^{-3}, (d) $N_{sub} = 10^{15}$ cm^{-3}, and (e) $N_{sub} = 10^{14}$ cm^{-3} at 300K. The arrow indicates the critical E_{eff} where phonon and surface roughness limited mobilities have the same value. The inset shows corresponding population of two lowest subbands.

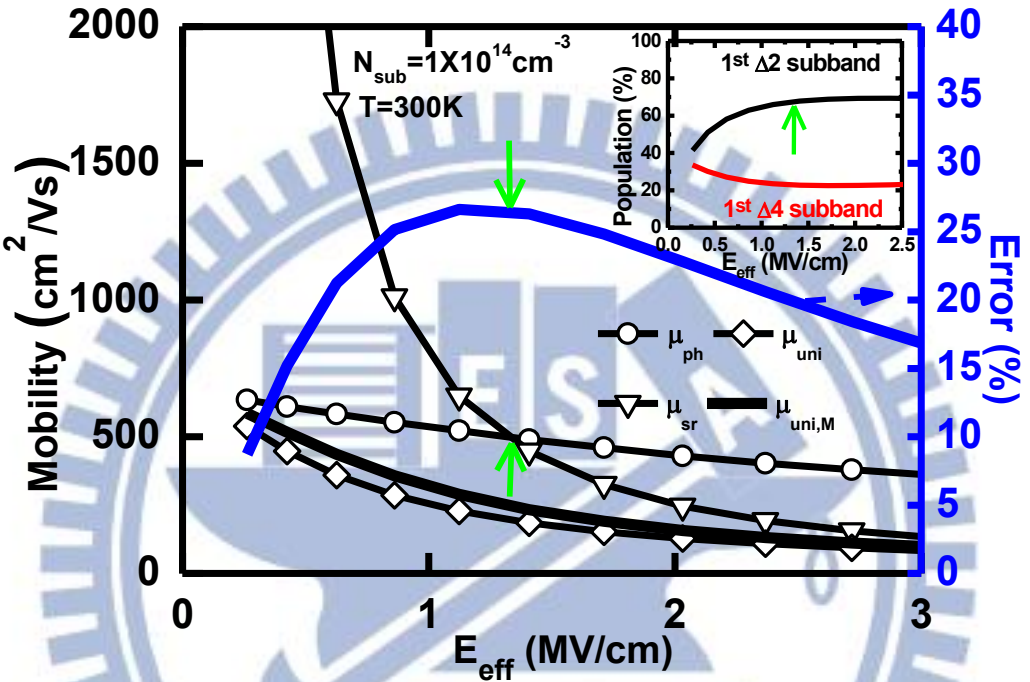

(e)

Figure 4.3 The apparent universal mobility (lines) obtained by Matthiessen's rule, simulated universal mobility, phonon limited mobility, and surface roughness limited mobility (lines with symbols) versus E_{eff} for (a) $N_{sub} = 5\times10^{17}$ cm^{-3}, (b) $N_{sub} = 10^{17}$ cm^{-3}, (c) $N_{sub} = 10^{16}$ cm^{-3}, (d) $N_{sub} = 10^{15}$ cm^{-3}, and (e) $N_{sub} = 10^{14}$ cm^{-3} at 300K. The arrow indicates the critical E_{eff} where phonon and surface roughness limited mobilities have the same value. The inset shows corresponding population of two lowest subbands.

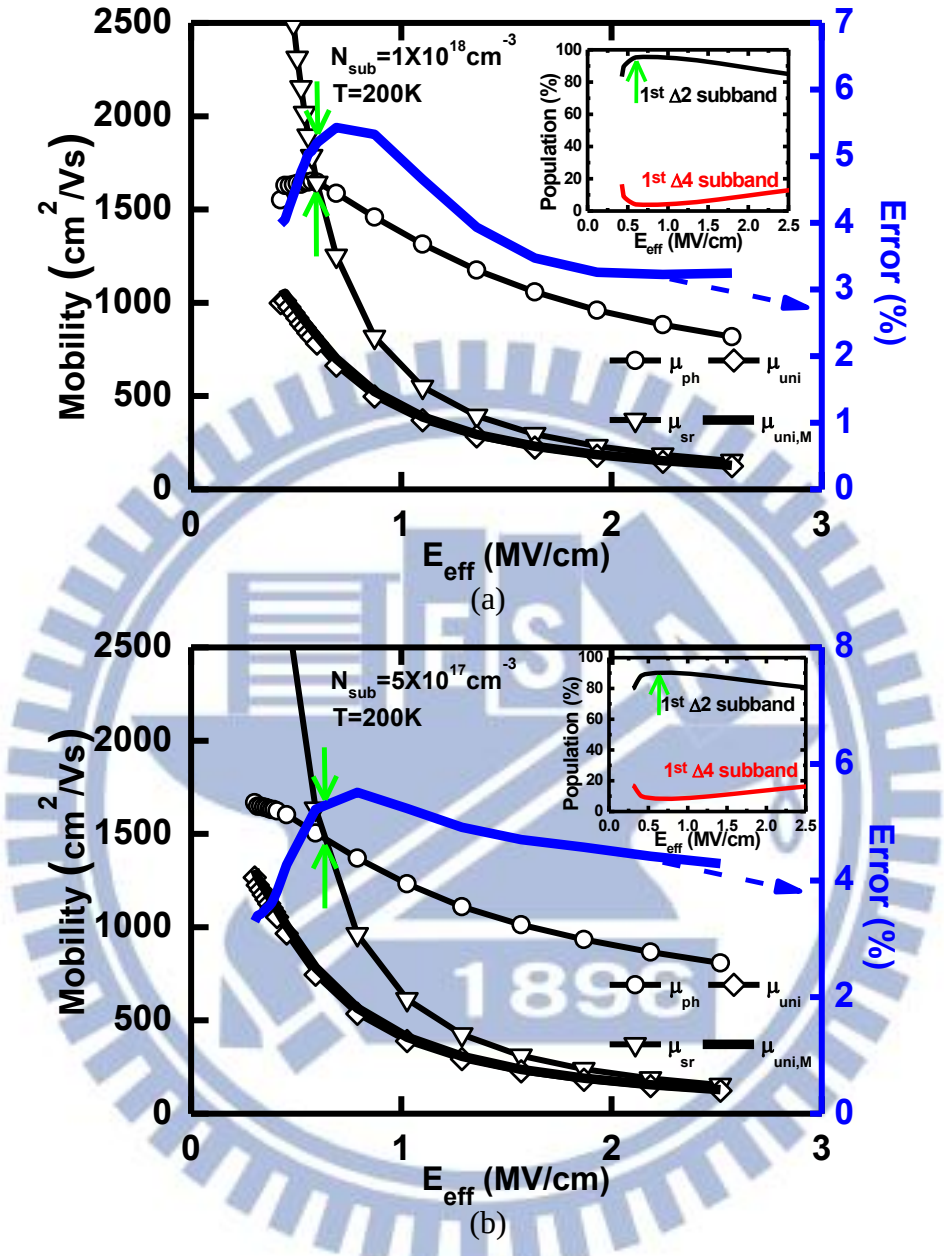

Figure 4.4 The universal mobility (lines) obtained by Matthiessen's rule, simulated universal mobility, phonon and surface roughness limited mobilities (lines with symbols) versus E_{eff} for (a) N_{sub} =10^{18} cm^{-3}, (b) N_{sub} = 5×10^{17} cm^{-3}, (c) N_{sub} = 10^{17} cm^{-3}, (d) N_{sub} = 10^{16} cm^{-3}, (e) N_{sub} = 10^{15} cm^{-3}, and (f) N_{sub} = 10^{14} cm^{-3} at 200K. The arrow indicates the E_{eff} where phonon and surface roughness limited mobilities have the same value. The inset shows corresponding population of two lowest subbands.

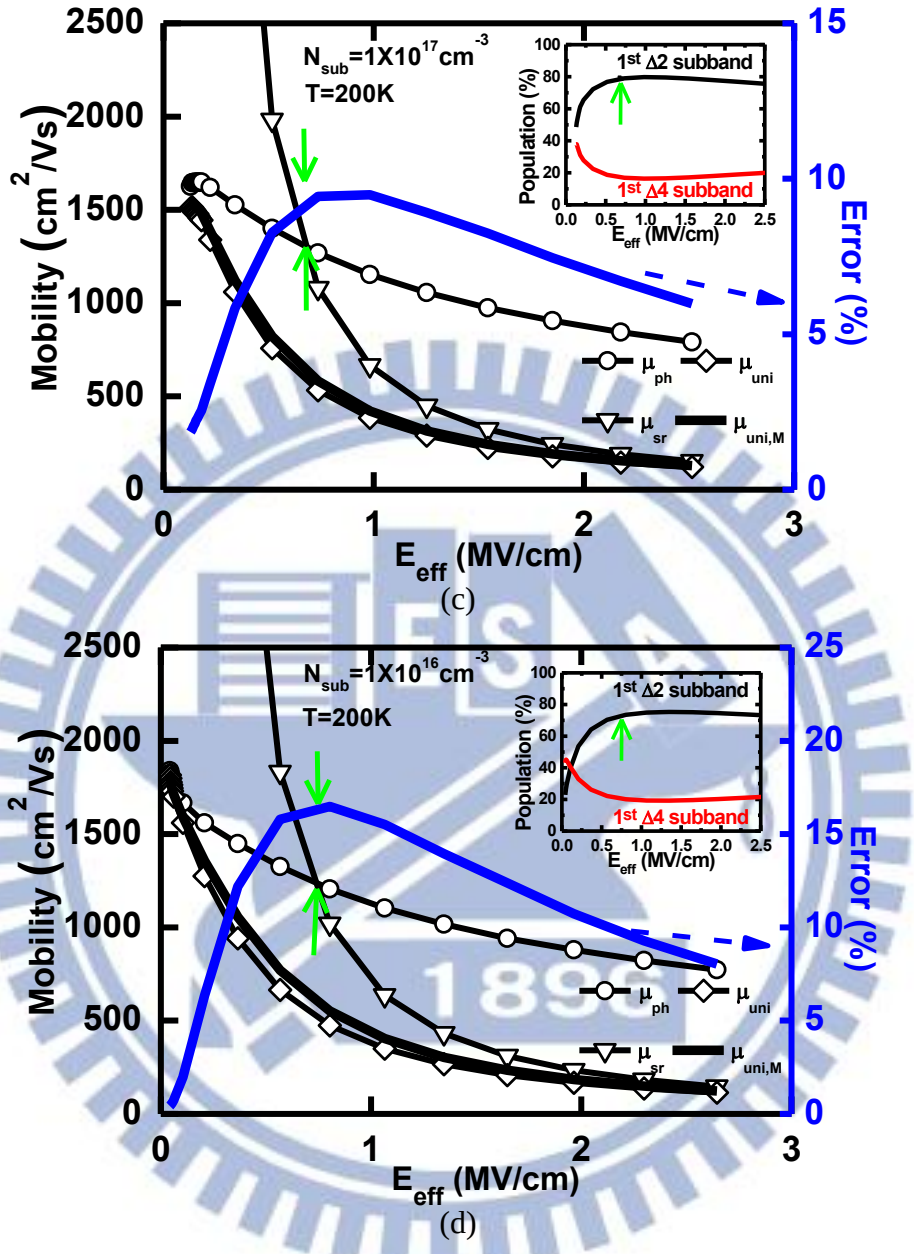

Figure 4.4 The universal mobility (lines) obtained by Matthiessen's rule, simulated universal mobility, phonon and surface roughness limited mobilities (lines with symbols) versus *Eeff* for (a) N_{sub} =10^{18} cm^{-3}, (b) N_{sub} = 5×10^{17} cm^{-3}, (c) N_{sub} = 10^{17} cm^{-3}, (d) N_{sub} = 10^{16} cm^{-3}, (e) N_{sub} = 10^{15} cm^{-3}, and (f) N_{sub} = 10^{14} cm^{-3} at 200K. The arrow indicates the *Eeff* where phonon and surface roughness limited mobilities have the same value. The inset shows corresponding population of two lowest subbands.

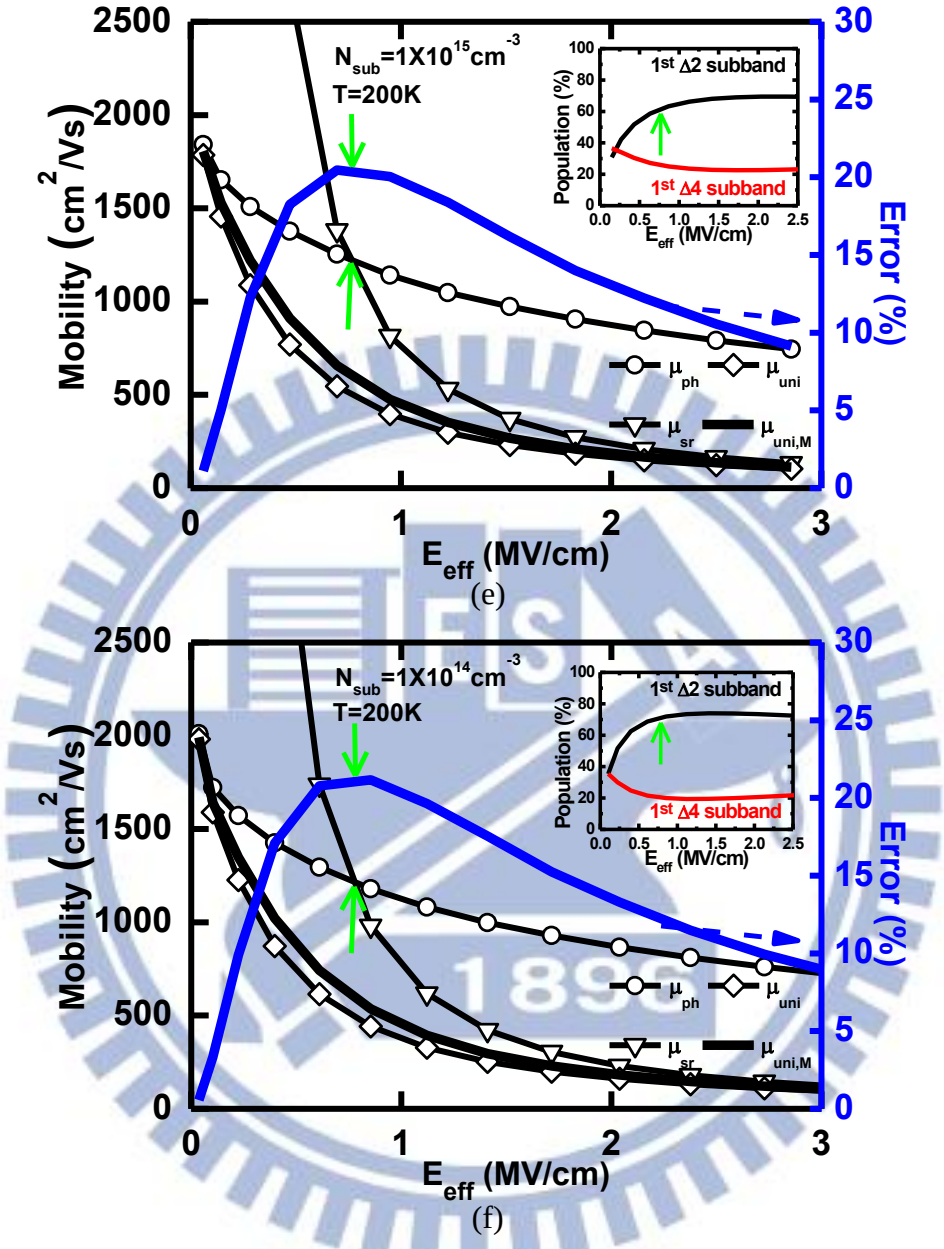

Figure 4.4 The universal mobility (lines) obtained by Matthiessen's rule, simulated universal mobility, phonon and surface roughness limited mobilities (lines with symbols) versus *Eeff* for (a) N_{sub} =10^{18} cm^{-3}, (b) N_{sub} = 5×10^{17} cm^{-3}, (c) N_{sub} = 10^{17} cm^{-3}, (d) N_{sub} = 10^{16} cm^{-3}, (e) N_{sub} = 10^{15} cm^{-3}, and (f) N_{sub} = 10^{14} cm^{-3} at 200K. The arrow indicates the *Eeff* where phonon and surface roughness limited mobilities have the same value. The inset shows corresponding population of two lowest subbands.

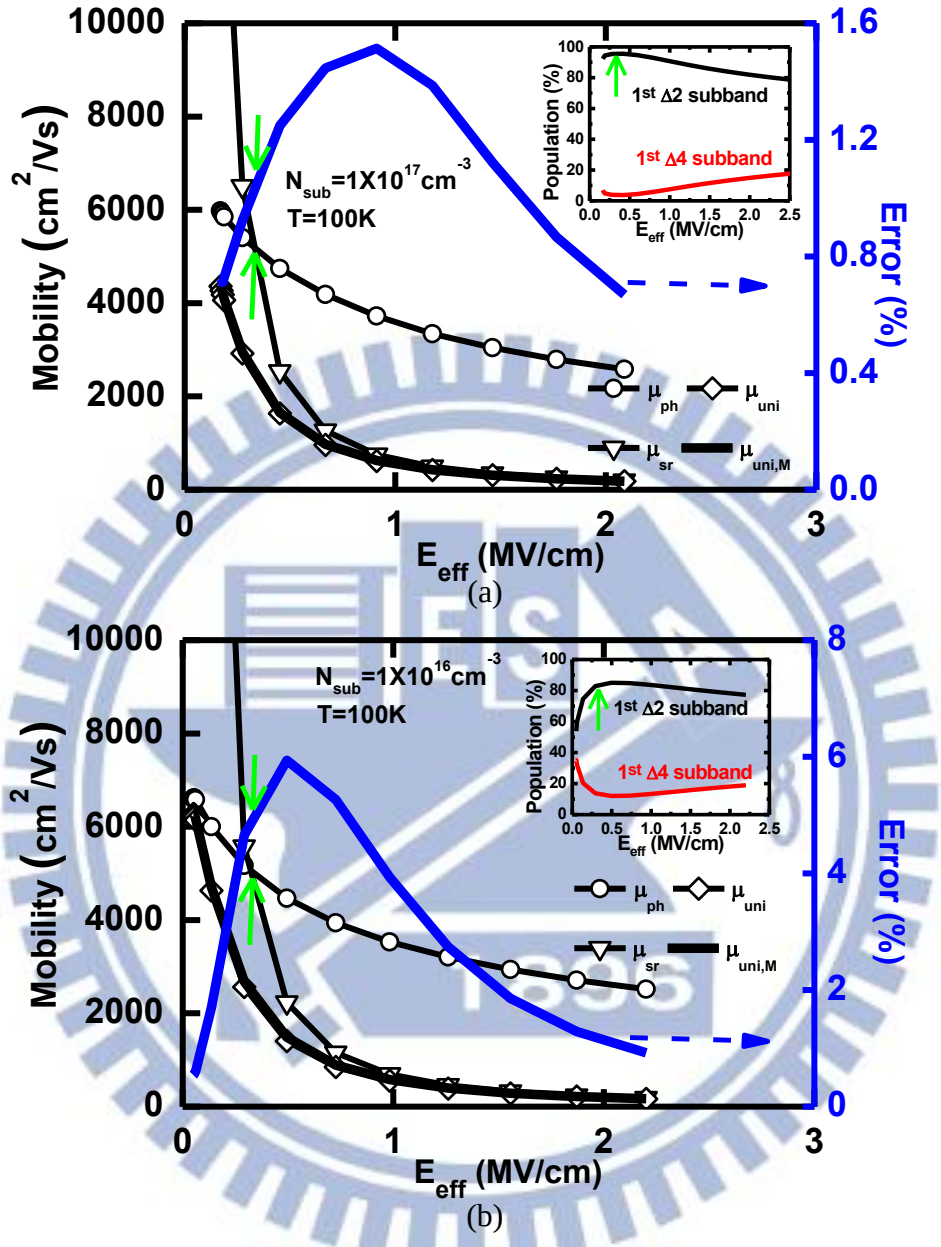

Figure 4.5 The universal mobility (lines) obtained by Matthiessen's rule, simulated universal mobility, phonon and surface roughness limited mobilities (lines with symbols) versus E_{eff} for (a) N_{sub} =10^{17} cm^{-3}, (b) N_{sub} = 10^{16} cm^{-3}, (c) N_{sub} = 10^{15} cm^{-3}, and (d) N_{sub} = 10^{14} cm^{-3} at 100K. The arrow indicates the E_{eff} where phonon and surface roughness limited mobilities have the same value. The inset shows corresponding population of two lowest subbands.

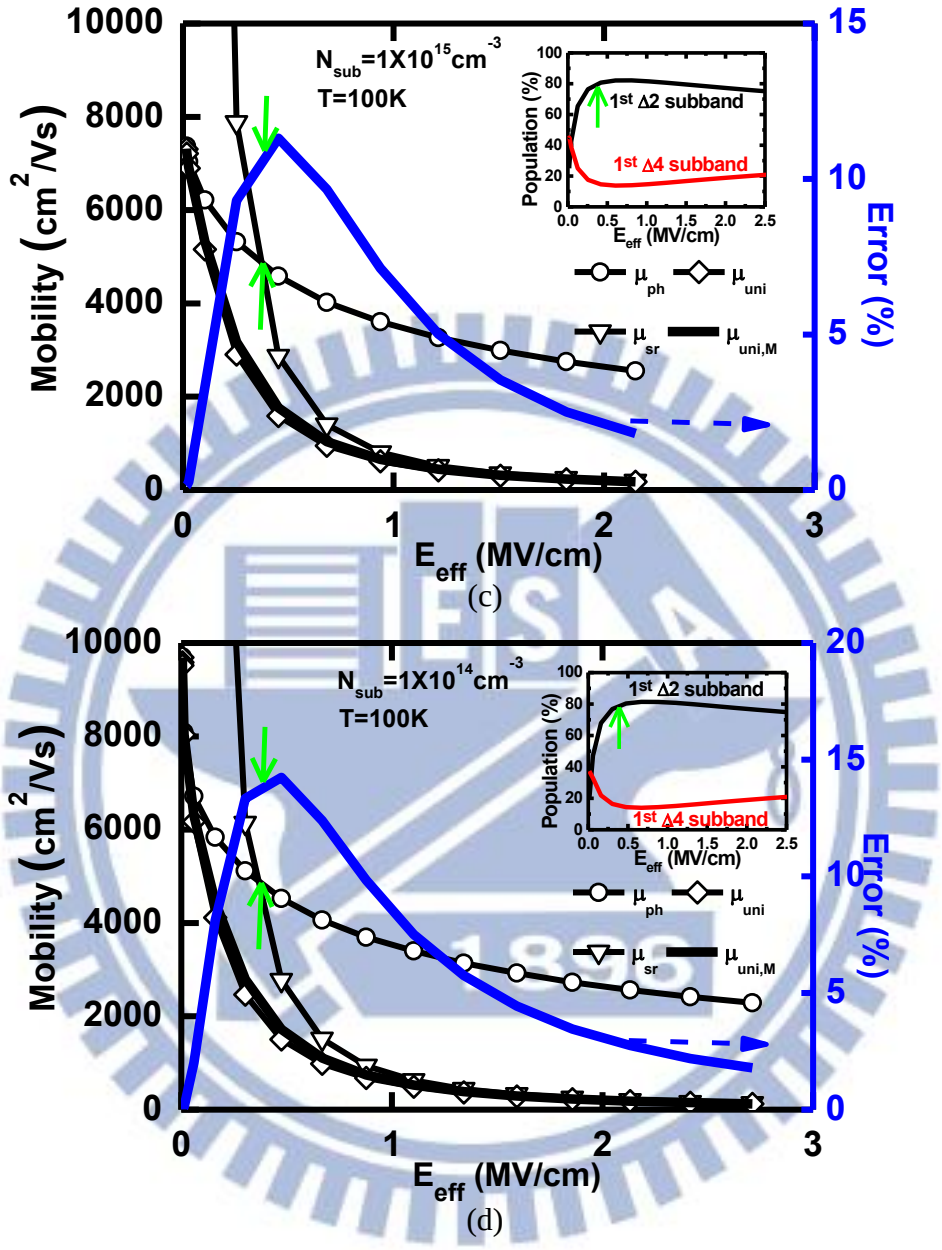

Figure 4.5 The universal mobility (lines) obtained by Matthiessen's rule, simulated universal mobility, phonon and surface roughness limited mobilities (lines with symbols) versus E_{eff} for (a) N_{sub} =10^{17} cm^{-3}, (b) N_{sub} = 10^{16}cm^{-3}, (c) N_{sub} = 10^{15} cm^{-3}, and (d) N_{sub} = 10^{14} cm^{-3} at 100K. The arrow indicates the E_{eff} where phonon and surface roughness limited mobilities have the same value. The inset shows corresponding population of two lowest subbands.

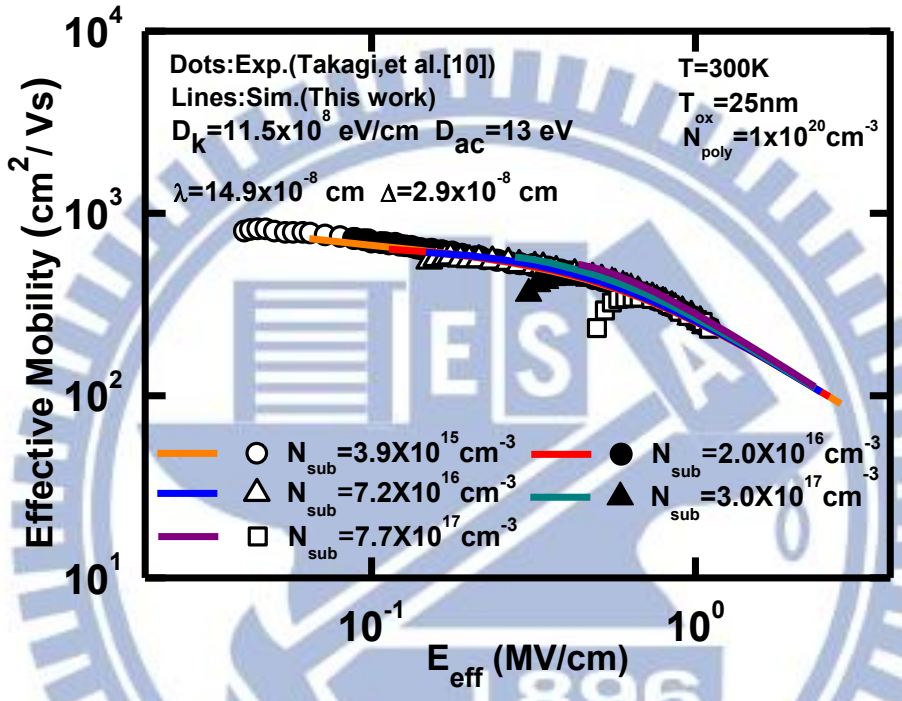

Figure 4.6 Electron effective mobility data (symbols) [10] for five substrate doping concentrations at 300K versus vertical effective electric field E_{eff}. Simulated universal mobility curves (lines) are shown. D_{ac} is the acoustic deformation potential; D_k is the deformation potential of the *k*-th intervalley phonon; λ is the surface roughness correlation length; and Δ is the surface roughness rms height.

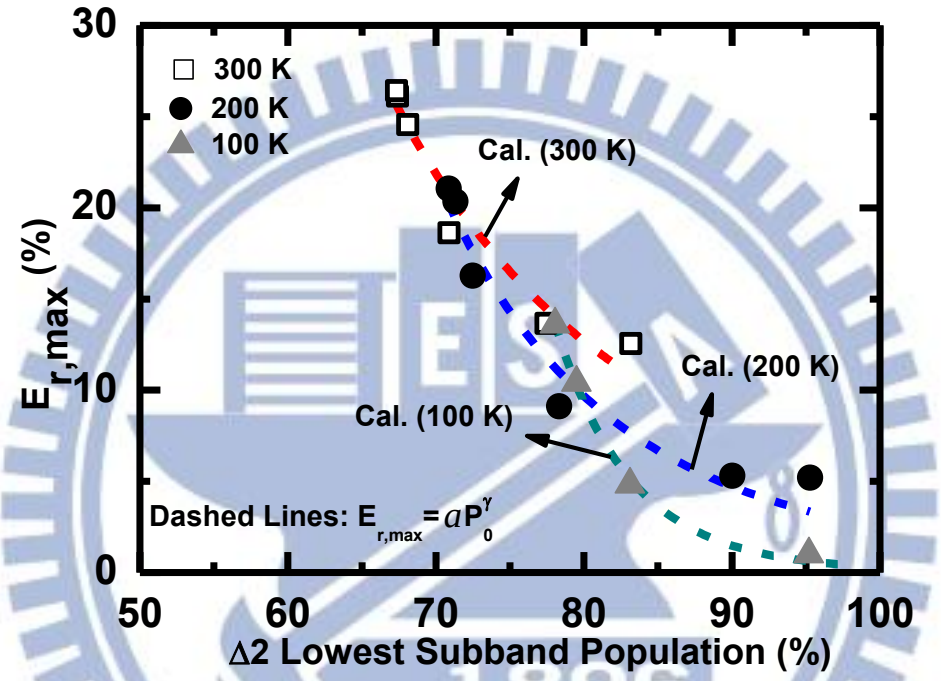

Figure 4.7 Scatter plot (symbols) of the simulated peak error and corresponding lowest subband population, created from different substrate doping concentrations (10^{14} cm^{-3} to 10^{18} cm^{-3}), with temperature as a parameter. The calculated results (dashed lines) using Eq. (4.2.4) are shown.

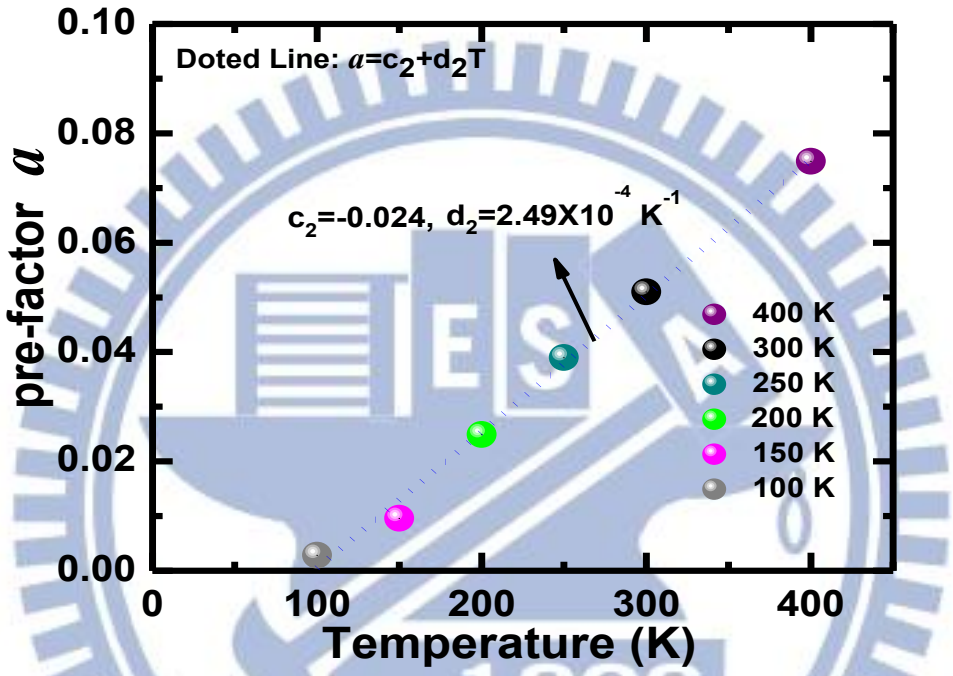

Figure 4.8 Extracted (symbols) pre-factor a in Eq.(4.2.4) versus temperature. The best fitting (dashed line) is shown.

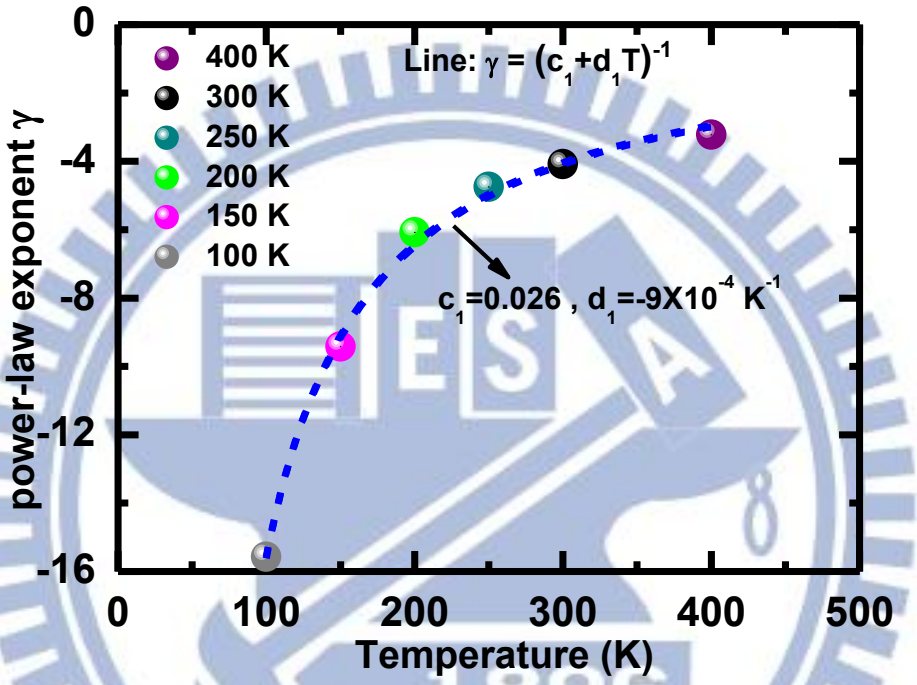

Figure 4.9 Fitted temperature (symbols) power-law exponent γ in Eq.(4.2.4) versus temperature. The best fitting (dashed line) is shown.

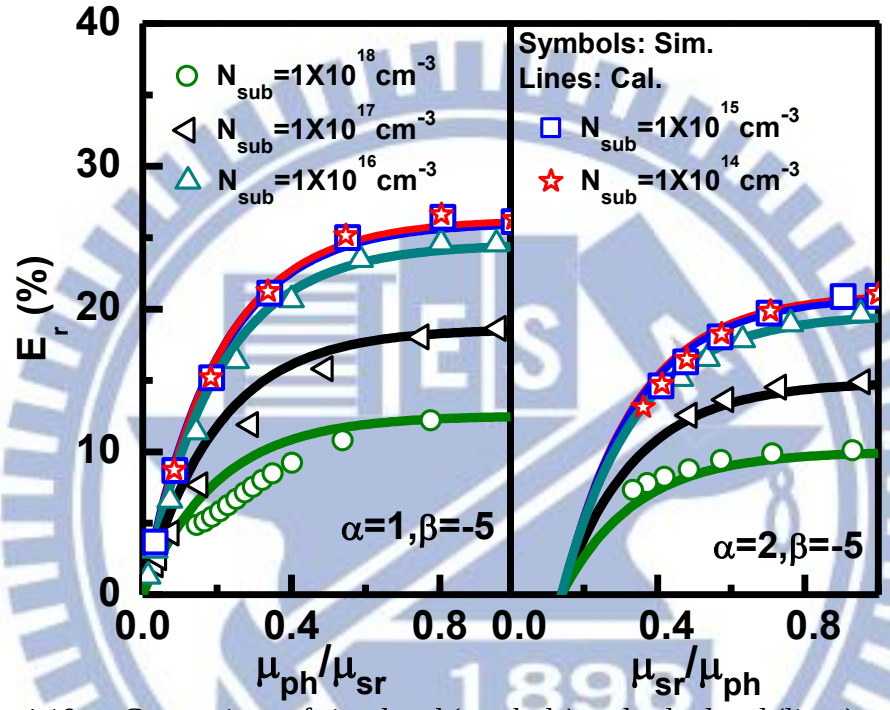

Figure 4.10 Comparison of simulated (symbols) and calculated (lines) errors for five different substrate doping concentrations at 300 K, plotted as a function of the ratio of phonon limited mobility and surface roughness limited mobility.

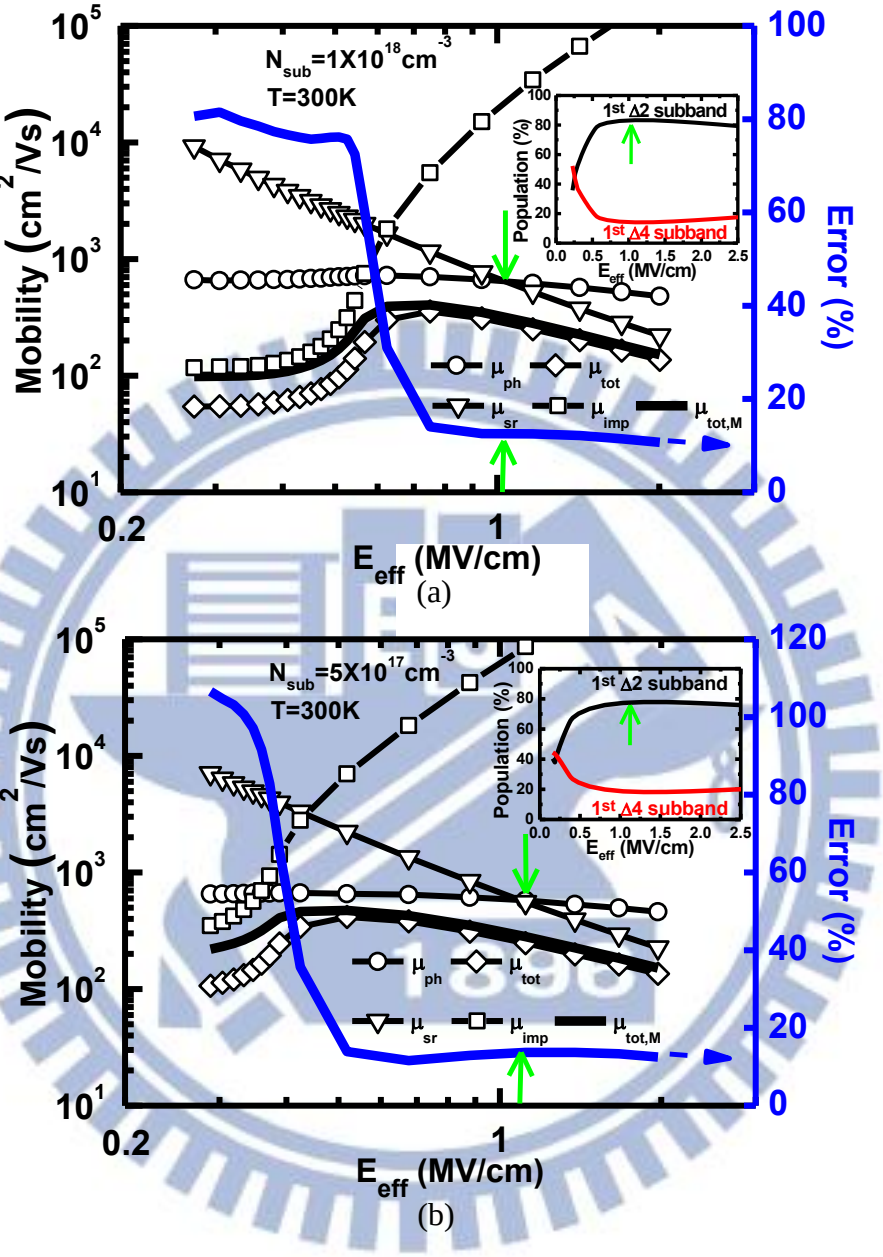

Figure 4.11 The total mobility (lines) obtained by Matthiessen's rule, simulated total mobility, phonon and surface roughness limited mobilities (lines with symbols) versus *Eeff* for (a) N_{sub} =10^{18} cm^{-3}, (b) N_{sub} = 5×10^{17} cm^{-3}, (c) N_{sub} = 10^{17} cm^{-3}, (d) N_{sub} = 10^{16} cm^{-3}, and (e) N_{sub} = 10^{15} cm^{-3} at 300K. The arrow indicates the *Eeff* where phonon and surface roughness limited mobilities have the same value. The inset shows corresponding population of two lowest subbands.

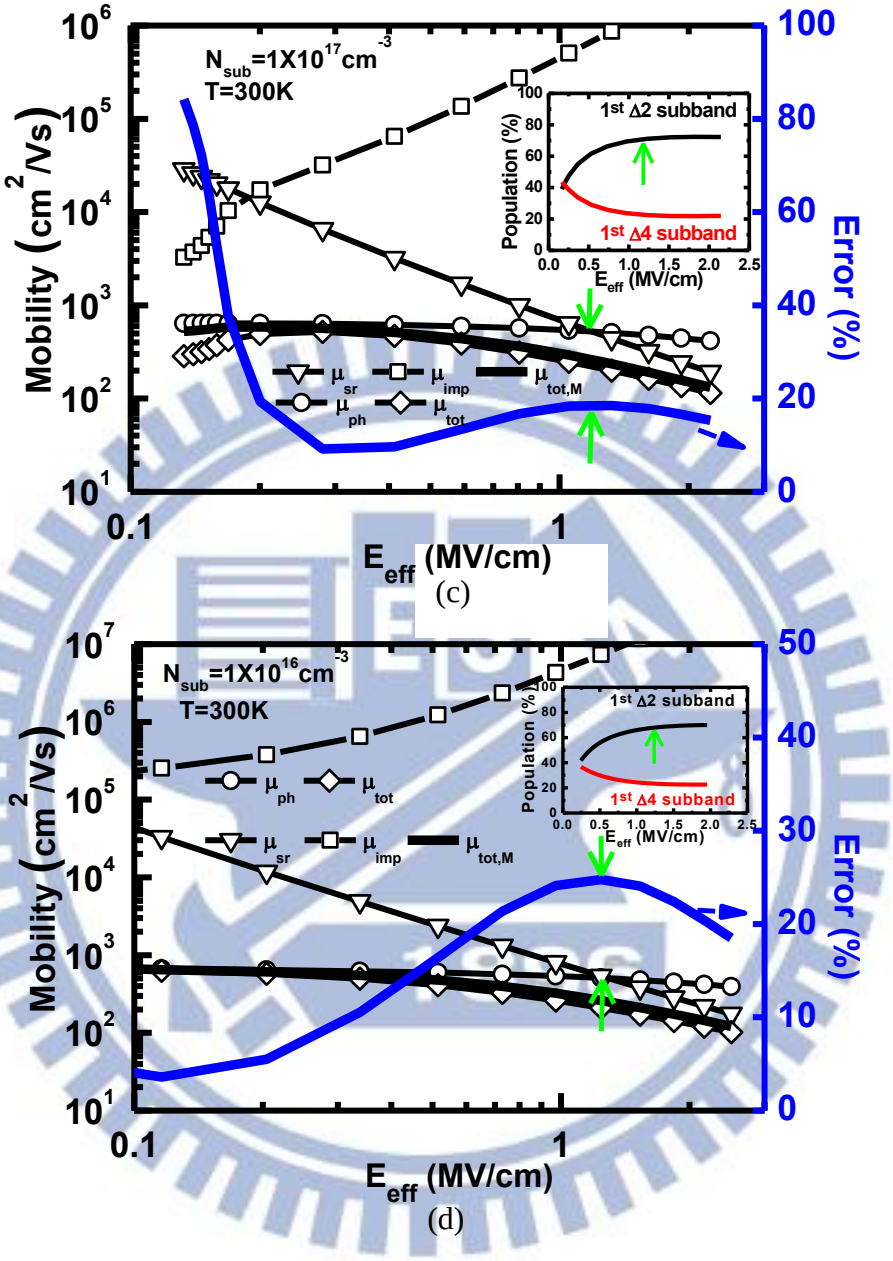

Figure 4.11 The total mobility (lines) obtained by Matthiessen's rule, simulated total mobility, phonon and surface roughness limited mobilities (lines with symbols) versus *Eeff* for (a) N_{sub} =10^{18} cm^{-3}, (b) N_{sub} = 5×10^{17} cm^{-3}, (c) N_{sub} = 10^{17} cm^{-3}, (d) N_{sub} = 10^{16} cm^{-3}, and (e) N_{sub} = 10^{15} cm^{-3} at 300K. The arrow indicates the *Eeff* where phonon and surface roughness limited mobilities have the same value. The inset shows corresponding population of two lowest subbands.

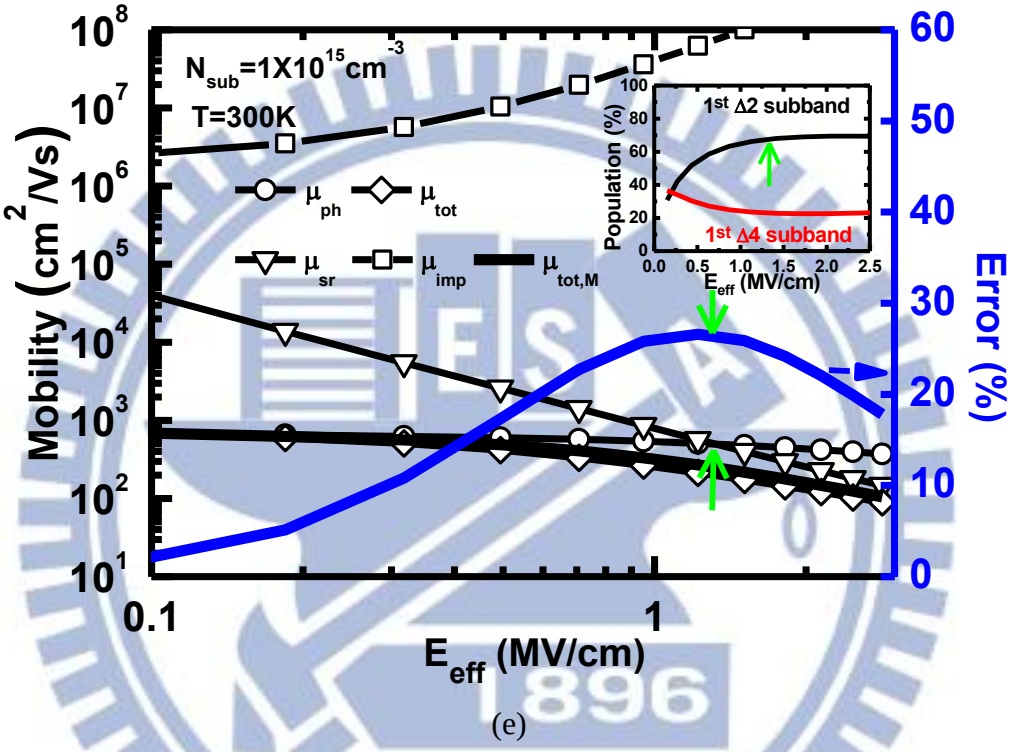

(e)

Figure 4.11 The total mobility (lines) obtained by Matthiessen's rule, simulated total mobility, phonon and surface roughness limited mobilities (lines with symbols) versus *Eeff* for (a) N_{sub} =10^{18} cm^{-3}, (b) N_{sub} = 5×10^{17} cm^{-3}, (c) N_{sub} = 10^{17} cm^{-3}, (d) N_{sub} = 10^{16} cm^{-3}, and (e) N_{sub} = 10^{15} cm^{-3} at 300K. The arrow indicates the *Eeff* where phonon and surface roughness limited mobilities have the same value. The inset shows corresponding population of two lowest subbands.

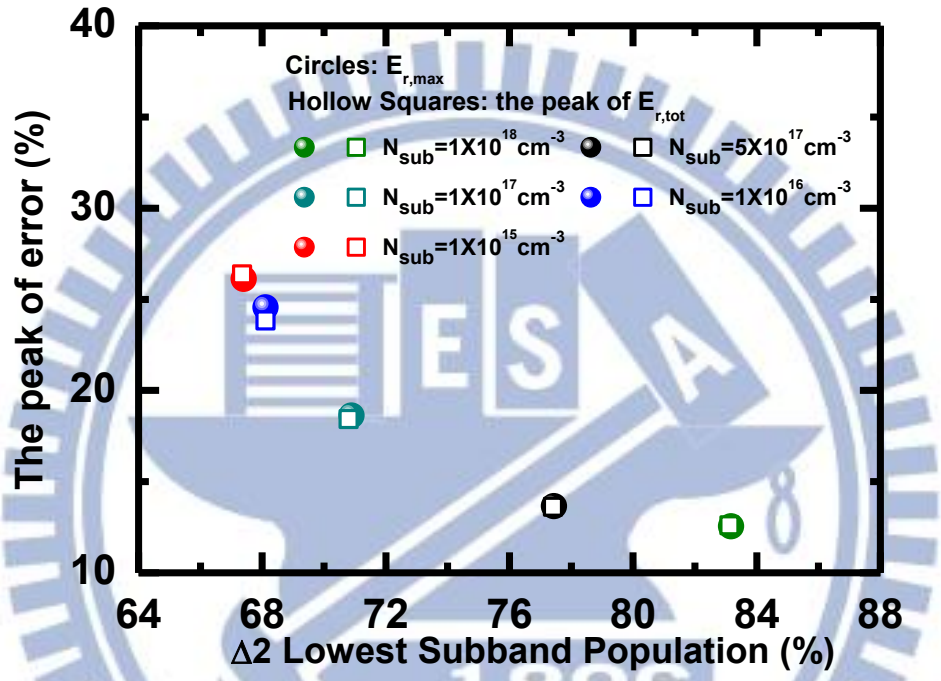

Figure 4.12 Scatter plot (symbols) of the simulated peak error $E_{r,max}$ and the peak of $E_{r,tot}$ (hollow squares) versus corresponding lowest subband population, created from different substrate doping concentrations (10^{15} cm^{-3} to 10^{18} cm^{-3}) at 300K.

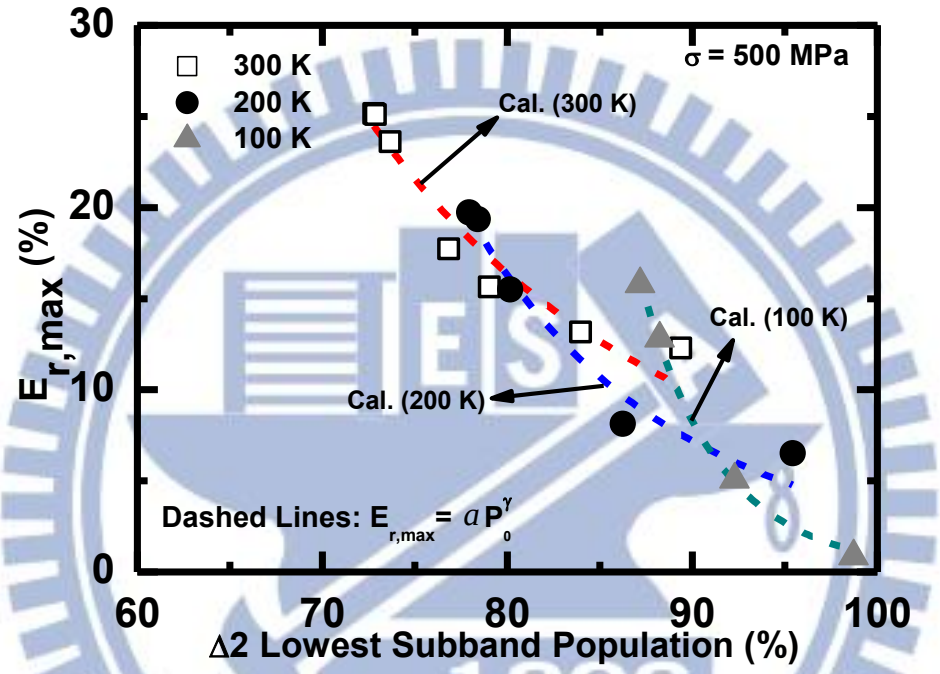

Figure 4.13 Scatter plot (symbols) corresponding to Figure 4.7 but under a uniaxial tensile stress of 500MPa. The calculation results (dashed lines) came from Eq.(4.2.4) with the pre-factor a =-0.018+ 2.69×10^{-4} T and the power-law exponent $\gamma = 1/(0.042 - 9\times10^{-4}\,T)$.

Electron Scattering and Physical Parameters for Si on (001)				
	This Work	Takagi[10]	Ferry[14]	A. Pirovano[15]
Acoustic phonon D_{ac} (eV)	13	12		
Optical phonon for Kth Intervally D_k (X10^8 eV/cm)	11.5	19.2	7-10	
Crystal density ρ (kg/cm^3)	2329	2329		
Sound velocity S_l (m/s)	9037	9037		
Surface Roughness Amplitude Δ (X10^{-8}cm)	2.9	2.6		1.6-2.5
The Correlation Length of surface Roughness λ (X10^{-8} cm)	14.9	14.9		10-20

Table I Electron scattering and physical parameters for Si used in this work and comparison with the literature values.